Hypersonic Boundary Layer Receptivity over a Blunt Cone to Freestream Pulse Disturbances

Simon He[*] and Xiaolin Zhong[†]

University of California, Los Angeles, California, 90095, USA

The receptivity of a 1.9 m long, 7-degree half-angle circular cone with a 9.525 mm nose radius at mach 10 to planar and axisymmetric freestream disturbances was investigated using a high-order shock-fitting method formulated for a perfect gas. After the meanflow was converged, unsteady Direct Numerical Simulations (DNS) were performed to study the receptivity of the flow to a variety of freestream disturbances with the same broadband, continuous frequency spectrum. These freestream disturbances were modelled as Gaussian pulses and include axisymmetric hotspot, fast acoustic, and slow acoustic pulse disturbances, as well as planar fast acoustic and slow acoustic pulse disturbances. The axisymmetric pulses were finite in three dimensions, while the planar disturbances were infinite in the y-z plane. Linear Stability Theory (LST) analysis was used to validate the unsteady DNS, study the receptivity mechanisms of the cone to the freestream pulses, and finally produce receptivity coefficients for the tested disturbances. Unsteady DNS results for the axisymmetric cases were found to agree well with the LST and indicated that the amplified 2nd mode instability corresponded the discrete mode F. All of the tested freestream pulse cases were shown to excite fast acoustic disturbances upstream of the 2nd mode region. The axisymmetric fast acoustic disturbance was found to generate the largest initial 2nd mode amplitudes, followed by the axisymmetric hotspot and then the axisymmetric slow acoustic pulse. The planar fast and slow acoustic pulses were also found to excite the 2nd mode, though these cases showed strong phase speed and growth rate modulations attributed to forcing waves. Spectral receptivity coefficient distributions were also produced. For the axisymmetric pulses, sampling location was shown to have little impact on the receptivity coefficients due to the negligible influence of forcing waves, while the planar acoustic cases saw large variations between disturbance sampling locations. The receptivity response for the axisymmetric disturbances was again strongest for the fast acoustic pulse, followed by the hotspot and then the slow acoustic pulse. For the planar pulses, the planar slow acoustic disturbance was found to have higher receptivity coefficients and to also fit the expected 2nd mode trend more closely.

I. Introduction

Understanding the process of high-speed boundary layer transition has been an enduring research goal in the hypersonics community. Transition to turbulence is known to dramatically increase aerodynamic drag and heating on the vehicle's surface as well as significantly affect the control of the vehicle.[1–3] Delaying transition and accurately predicting its behavior in hypersonic vehicles will allow for greater specificity in the design of thermal protection systems (TPS). This in turn would help minimize the weight impact of TPS, allowing for expanded payload capacities and improved overall performance of hypersonic vehicles.

Hypersonic boundary layer transition is governed by several mechanisms and can be broken down into three distinct stages: (i) boundary layer receptivity, (ii) linear growth of small amplitude instabilities, and (iii) nonlinear breakdown of the at finite disturbance amplitudes.[4] Traditionally, studies on laminar-turbulent transition at hypersonic speeds have been focused on the linear growth of Mack[5] modes, for which the 2nd mode instability has been found to dominate in hypersonic speeds. Fedorov[1] recently described these instability modes as acoustic rays trapped between the wall and sonic line in the boundary layer. Depending

---

*Graduate Student, Mechanical and Aerospace Engineering, simon.he.ucla@gmail.com, AIAA Student Member.
†Professor, Mechanical and Aerospace Engineering, xiaolin@seas.ucla.edu, AIAA Associate Fellow.

American Institute of Aeronautics and Astronautics

on flow geometry, resonant interactions can occur between these disturbance modes at different points along the domain and cause instability.[3] This study focuses on the receptivity mechanisms associated with weak environmental forcing (stage i), which are commonly encountered in both real flight and experimental conditions, and the linear instability growth that this forcing excites (stage ii). Figure 1 provides a schematic diagram depicting the general receptivity process in hypersonic flow over a blunt body.
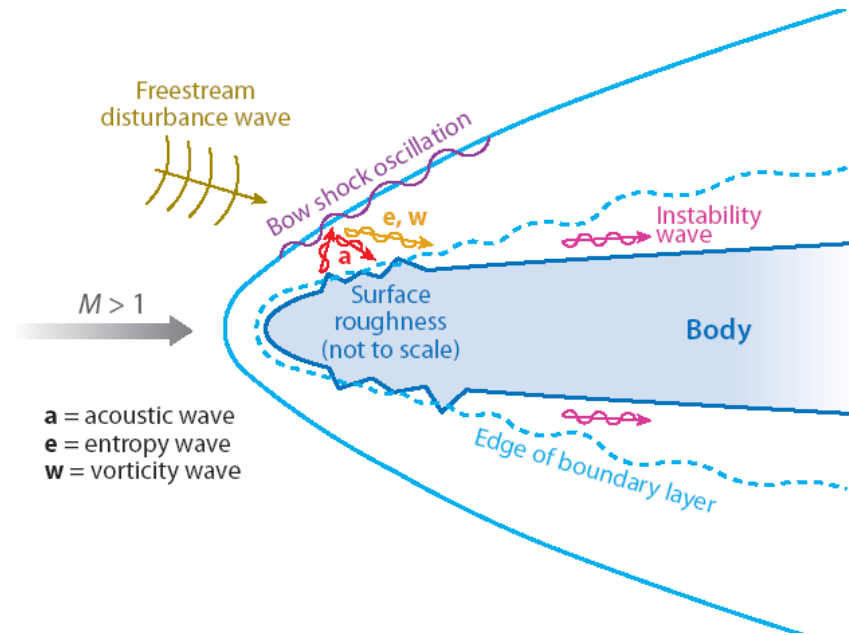

Figure 1. Schematic diagram of freestream receptivity.[3]

Receptivity mechanisms dictate the initial amplitudes of disturbances in the boundary layer that result from environmental forcing, which greatly impacts the general stability behavior of the flow. The receptivity of hypersonic boundary layers to freestream acoustic disturbances has been extensively studied in hypersonic flows over flat plate[4, 6–9] and cone geometries.[10–13] For a flat plate case, Ma and Zhong[4, 6, 7] found that freestream acoustic disturbances generate initially stable modes near the leading edge, which then become unstable after synchronization. This synchronization point is where the discrete modal disturbances originating from the continuous freestream fast and slow acoustic spectra interact and exchange energy, which can eventually destabilize one of the discrete modes to cause an amplifying Mack mode instability. Ma and Zhong[4] labeled the discrete modes originating from the freestream fast acoustic spectrum as mode I, II, etc. continuing downstream in accordance with their appearance, while they labeled the disturbances originating from the freestream slow acoustic spectrum as the 1st mode, 2nd mode, and so on in accordance with the Mack mode instabilities. Based on their asymptotic leading edge behavior, Fedorov and Tumin[14] renamed the discrete acoustic modes emerging from the continuous fast acoustic spectrum sequentially as mode F1, F2, etc... (described by Mack as the multiple-viscous solutions[15]). Similarly, mode S referred to the discrete slow acoustic mode originating from the continuous slow acoustic spectrum and corresponds to the Mack mode instabilities presented in Ma and Zhong.[4] It has been found that, depending on flow conditions, both mode F and mode S instabilities are capable of becoming unstable.

In their studies, Ma and Zhong[4] found that freestream acoustic, vorticity, and entropy waves modelled as discrete fourier modes could all excite modal disturbances in flat plate boundary layers. They showed that a freestream entropy disturbance excited strong stable mode I (F1) disturbances upstream on the flat plate. These waves would then be converted into mode II (F2) mode instabilities by synchronization, though the disturbance modulations were found to be relatively weak near synchronization. The freestream fast acoustic disturbance, however, experienced significantly stronger modal interaction after synchronization. Furthermore, the freestream slow acoustic disturbance was shown to successfully excite an unstable 2nd mode, which was found to be the discrete mode S by LST, while the fast acoustic disturbance became a strong mode II (F2) disturbance downstream of synchronization. This indicates very different receptivity paths for these different disturbance types, and necessitates a wide parametric space of disturbances in order

American Institute of Aeronautics and Astronautics

to fully characterize the receptivity response of a flow. Ma and Zhong[4,7] also found that the acoustic waves in the shock layer, which resulted from shock-disturbance interactions, would be reflected by the boundary layer and generate secondary acoustic, entropy, and vorticity disturbances after additional shock interactions. The resulting combined disturbances greatly effected the receptivity of the boundary layer in their flat plate.

Fedorov has also conducted both theoretical and numerical studies on the receptivity of flat plate boundary layersl. Fedorov's[8] theoretical treatment focused on the mechanisms associated with the scattering and diffraction of acoustic waves near the leading edge of a flat plate. He found that the dominant mechanism in leading edge receptivity behavior varied between scattering and diffraction oeffects depending on wave incidence angles, and that leading edge receptivity could result in stronger disturbances than intermodal exchanges for flat plate geometries. The numerical study by Fedorov et a.[9] focused on the receptivity of a flat plate to temperature spot disturbances induced both in the freestream upstream of the shock, and near the boundary layer behind the shock. When the temperature disturbance was imposed directly on the boundary layer, they found that a discrete mode F was generated. This mode then experienced intermodal interactions, exciting the unstable mode S. The conventional freestream disturbance instead excited acoustic waves through shock-disturbance interactions, which then propagated through the boundary layer and excited the unstable mode S disturbance. They found that this shock-disturbance interaction generated perturbation amplitudes that were an order of magnitude higher than those associated with the pure boundary layer disturbance.

Several numerical studies on the receptivity behaviors of conical geometries have also been performed. Zhong and Ma[16] performed a numerical study of the receptivity of a blunt cone with discrete fast acoustic waves at Mach 7.99. Contrary to what they observed for the flat plate case[4,7] the boundary layer disturbances were initially highly oscillatory near the nose, but became dominated by 2nd mode instabilities downstream of synchronization, even though the 2nd mode corresponded to mode S in this case. This receptivity process was significantly different to what they had found for a flat plate case, indicating that geometry plays a significant role in receptivity. They further pointed out how factors such as bow shock interactions, nose bluntness, and entropy layer instabilities could affect the receptivity mechanisms for blunt cones when compared to flat plates.

Similarly, Balakumar and Kegerise[10] found that both vortical and acoustic disturbances excited the 2nd mode instability in cones, and that the receptivity response was stronger for acoustic disturbance waves. They also reported that wave incidence had some effect on the receptivity response, indicating a need to account for more complex disturbance conditions to fully approximate the envelope of conditions found in flight. Kara et al.[12] and Lei and Zhong[17] attempted to use receptivity calculations to predict transition on sharp and blunt cones. They found that while freestream waves readily generated 2nd mode instabilities downstream on the cone, 2nd mode amplification was unable to accurately predict the transition behavior observed in blunt cone experiments. Possible explanations for this include non-modal disturbance growth, such as transient growth,[18] or a failure to accurately capture the effects of freestream environmental noise.[17]

Past studies investigated receptivity by using planar freestream disturbances modelled as discrete fourier modes.[4,10] However, continuous broadband disturbances from the freestream would more accurately represent noise environments found both in actual flight and experiment.[19] Balakumar and Chou[11] approximated these broadband frequency disturbances through carefully chosen combinations of discrete two-dimensional planar slow acoustic waves. The amplitudes of each of the wave disturbances in the packet was determined by equating the energy of each discrete wave with a chosen frequency in the experimentally measured freestream noise spectrum. They found that doing so allowed the transition location to predicted with a reasonable accuracy for the sharp nose cases, though the accuracy of the threshold criterion they used decreased significantly for the blunter cone. They also found that larger nose bluntness decreased receptivity coefficients, which was defined as the wall pressure perturbation at the neutral point normalized by the freestream acoustic noise level.

Huang[20,21] instead modeled a broadband disturbance through the use of an axisymmetric freestream hotspot over a compression cone, and found that this hotspot was effective in exciting 2nd mode instabilities in the boundary layer. Huang found that the resulting disturbance growth rate and phase speed compared well to LST, and corroborated the results from the experimental study the simulation was based on. The receptivity mechanism for the entropy spot over a compression cone was also found to be very similar to that of discrete acoustic waves over a blunt cone, but different from entropy spot disturbances for flat plates. This further reinforces the significance of geometry for receptivity mechanisms. Huang was then able to use the LST-derived N-factors along with the surface perturbations from the unsteady DNS to calculate the

American Institute of Aeronautics and Astronautics

receptivity coefficients for the 2nd mode disturbance. This was done by sampling the total DNS boundary layer perturbation at a point inside the LST-predicted 2nd mode region, and then normalizing the DNS data by the N-factor corresponding local N-factor to extract the initial 2nd mode perturbation amplitude. He found that this process was successful in isolating the receptivity response of the 2nd mode disturbance, even though the total disturbance was highly multimodal.[21] Furthermore, he was also able to extract the phase angle spectrum of the resulting boundary layer disturbances. With these results, initial boundary layer disturbances for this particular case should be able to be reconstructed. While these studies showed that Gaussian pulses could successfully approximate continuous frequency spectrum disturbances and also excite significant modal instabilities in hypersonic flows over cones, they were very limited in the disturbances they considered. Additional investigation into the receptivity of acoustic waves must also be made as experimental environments are often dominated by acoustic noise as well.[22] Further expanding the receptivity database to include acoustic and vorticity disturbances, as well as more complex three-dimensional disturbances will be necessary in order to fully categorize the response of the flow to the freestream noise conditions that may be found in experiment and in flight.

LST has historically been used to track the spatial and temporal development of discrete instability modes, though parabolized stability equations (PSE) have also risen in prominence recently to account for nonparallel and nonlinear effects.[23] Current transition prediction procedures, such as the e^N method, rely on using growth rates for these modal instabilities derived from LST or PSE to determine the relative amplification of the disturbance amplitudes. Empirically determined threshold values are then used to predict the onset of turbulent transition.[11, 24, 25] This prediction approach assumes that the boundary layer disturbances operate solely in the linear growth regime of transition and ignore the effects of both nonlinear interactions and receptivity mechanisms on the flow. Essentially, these schemes assume that the transitionary behavior of the flow is governed solely by linear growth. While this assumption can provide good internal consistency in a given environment, transition thresholds based on this methodology often vary significantly between different experiments. Schneider[19] described similar experiments with threshold N-factors of 5 and 8, demonstrating the potential impact of noise environments on transition. This freestream noise comes primarily in the form of acoustic waves radiated from turbulent boundary layers on experimental tunnel walls.[22, 26] Thus, neglecting the initial amplitudes generated by receptivity mechanisms prevents a more general application of transition prediction results.

Receptivity data has potential applications in several areas. For instance, the initial disturbance amplitudes derived from receptivity studies can be used to provide initial forcing conditions to nonlinear breakdown studies such as Sivasubramanian's and Fasel's.[27] These studies simulate the nonlinear interactions of finite amplitude disturbance modes in the boundary layer and investigate how these mechanisms can also lead to turbulence outside of the linear growth regime. Similarly, more robust transition estimation schemes require a combined consideration of both receptivity mechanisms and linear instability growth to improve their accuracy. Crouch[24] proposed a variable N-factor method that corrects the traditional e^N method through fitting a variation of the N-factor with a simplified model of the freestream response. This has the advantage of requiring no additional computations after the receptivity data and linear growth (N-factor) data are first obtained. Another improved transition model is based on the amplitude method proposed by Mack,[28] which also uses receptivity data to correlate initial disturbance amplitudes to freestream noise environments. Marineau[29] used this amplitude method, experimental receptivity correlations, and simulation results in an iterative process to estimate transition on a selection of sharp and blunt nosed cones. He showed that this method could predict transition for blunt cones and cones at angle of attack much more accurately than more traditional e^N methods. Ustinov[30] also extended this amplitude method to investigate laminar-turbulent transition on a swept wing using a combined amplitude criterion for steady state and time dependent perturbations in the flow. He found that this method successfully reproduced experimentally observed dependencies on Reynolds number, local surface roughness, and freestream turbulence. The receptivity results applied in Crouch's and Marineau's studies used empirical, experimentally fitted receptivity correlations. Utilizing receptivity spectra derived from DNS simulations would provide improved precision to the initial amplitude calculations and potentially help to further improve the accuracy of these alternative transition prediction methods.

Finally, while the method used by Huang[21] is able to isolate the 2nd mode response to freestream forcing, the multimodal nature of boundary layer disturbances indicates that this also ignores a large spectrum of other perturbations that can contribute significantly to transition. Therefore, understanding the receptivity response of all of the instability modes in the flow will be necessary to apply these results to transition

prediction. More rigorous modal decomposition methods, such as the bi-orthogonal decomposition used by Tumin[31] and Miselis[32] can be used to decompose the receptivity spectra into components associated with the discrete and continuous modal instabilities found in the boundary layer and allow these individual modes to be studied in more detail. This rigorous modal decomposition would provide additional much needed insight into the physics of hypersonic flows over aerodynamic geometries.

The current study expands on previous work by Huang[20, 21] through the inclusion of additional freestream disturbance types in order to generate a more complete view of the broadband receptivity behavior of cones to continuous, broadband frequency freestream disturbances. The receptivity mechanisms for the axisymmetric fast acoustic, slow acoustic, and hotspot freestream pulses have been studied alongside the planar fast and slow acoustic pulses. This work aims to use steady and unsteady DNS along with LST to study the effects of freestream pulse disturbances of varying complexity on a straight cone. The goal is to then use these DNS and LST results to generate receptivity coefficients for the 2nd mode disturbance for each of these conditions, and provide a database of the initial disturbance response to freestream noise. This database would be directly applicable for future transition prediction and nonlinear breakdown studies.

II. Simulation Conditions

This study aims to expand on previous work by Huang and Zhong[20, 21] which detailed the receptivity response of flow over a flared cone at Mach 6 to freestream hotspot pulses, and used a combination of LST and unsteady DNS to generate receptivity coefficients. The current study focuses on the receptivity of a 9.525 mm nose radius circular, straight cone with a half-angle of 7 degrees at mach 10 to freestream axisymmetric fast acoustic, slow acoustic, and hotspot pulse disturbances as well as freestream planar fast and slow acoustic disturbances. The perturbations were modelled as Gaussian pulses in the freestream, providing for continuous, broadband frequency disturbances. Additionally, the cone studied here was 1.9m in length. The DNS simulations used 240 points in the wall-normal direction and roughly five points per millimeter on the surface of the cone in the streamwise direction. In the azimuthal direction, four points are used for the base axisymmetric flows. The flow conditions for this study are summarized in Table 1 and are based on the tunnel conditions reported by Marineau[33] for run 3752.

Table 1. Freestream flow conditions for DNS simulations.

Parameter	Value	Parameter	Value
M_∞	9.79	$h_{0,\infty}$	1.07 MJ/kg
ρ_∞	4.27 E-2 kg/m^3	p_∞	0.65 kPa
T_∞	51.0 K	U_∞	1426 m/s
$T_w/T_{0,\infty}$	0.3	Pr	0.72
Re/m (1E6/m)	18.95	$Angle\ of\ Attack$	0°

The DNS code used in this study utilizes a shock-fitting formulation with the parameters in Table 1 defining the freestream conditions upstream of the shock formed over the body. Marineau et al.[33] used curve fits of experimental data to generate the viscosity used for the Reynolds number calculations instead of Sutherland's Law. This lead to approximately a 10% difference in the calculated freestream unit Reynolds numbers between this study and Marineau's.

The meanflow was first converged with the steady DNS, after which the pulse disturbances were introduced in the freestream. The unsteady DNS was then run until the pulse and any resulting perturbations were convected out of the meanflow domain, after which a Fast Fourier Transform (FFT) was used to decompose the surface pressure perturbation data for each disturbance case into their frequency spectra. The meanflow was also used in LST to identify modal instabilities in the flow. The FFT decomposed data was then normalized with LST-derived N-factors in order to produce receptivity coefficient spectra for the primary 2nd mode disturbance for each case.

American Institute of Aeronautics and Astronautics

III.   Governing Equations

The solution methods for the DNS and LST codes were originally developed and implemented by Ma and Zhong[4, 34] and are formulated for a perfect gas. This assumption was made based on the low freestream stagnation enthalpy reported in Table 1. Their formulation is highlighted here for clarity. The three-dimensional Navier-Stokes equations in conservative form consist of a single species mass conservation equation, three momentum conservation equations, and the energy equation. The governing equations in vector form are written as

$$\frac{\partial U}{\partial t} + \frac{\partial F_j}{\partial x_j} + \frac{\partial G_j}{\partial x_j} = 0, \quad (j = 1, 2, 3) \tag{1}$$

where U is the state vector of conserved quantities and F_j and G_j are the inviscid and viscous flux vectors, respectively. Here, the j indices indicate Cartesian coordinates in the streamwise, radial, and azimuthal directions about the cone. The conservative vector U is comprised of five conservative flow variables for mass, momentum, and energy:

$$U = \begin{bmatrix} \rho & \rho u_1 & \rho u_2 & \rho u_3 & e \end{bmatrix}^T \tag{2}$$

Additionally, the inviscid F_j and viscous G_j flux vectors are written as:

$$F_j = \begin{bmatrix} \rho u_j \\ \rho u_1 u_j + p\delta_{1j} \\ \rho u_2 u_j + p\delta_{2j} \\ \rho u_3 u_j + p\delta_{3j} \\ (e + p)u_j \end{bmatrix} \tag{3}$$

$$G_j = \begin{bmatrix} 0 \\ \tau_{1j} \\ \tau_{2j} \\ \tau_{3j} \\ \tau_{jk}u_k - q_j \end{bmatrix} \tag{4}$$

Since this study assumes a perfect gas flow, the equation of state and the transport equations are

$$p = \rho RT \tag{5}$$

$$e = \rho(C_v T + \frac{1}{2}u_k u_k) \tag{6}$$

$$\tau_{ij} = \mu\left(\frac{\partial u_i}{\partial x_j} + \frac{\partial u_j}{\partial x_i}\right) - \lambda\frac{\partial u_k}{\partial x_k}\delta_{ij} \tag{7}$$

$$q_j = -\kappa\frac{\partial T}{\partial x_j} \tag{8}$$

Furthermore, the viscosity coefficent μ is calculated through Sutherland's law for nitrogen gas

$$\mu = \mu_r \left(\frac{T}{T_0}\right)^{\frac{3}{2}} \frac{T_r + T_s}{T + T_s} \tag{9}$$

In these equations R is the gas constant while c_p and c_v are the specific heats, which are assumed to be constant for a given ratio of specific heats γ. The coefficient λ is assumed to be $-2\mu/3$ and the heat conductivity coefficient κ is computed through a fixed Prandtl number of 0.72.

American Institute of Aeronautics and Astronautics

IV. Numerical Methods

A. DNS

The DNS code utilizes a high-order shock-fitting method for a perfect gas flow that was developed and validated extensively by Zhong[4, 34] to compute the flow field between the shock and the body. The numerical method is summarized here for clarity. For shock-fitting computations the shock location is treated as an additional unknown, so its position is solved along with the flow field. Since the shock position is not stationary, the grid used to compute the flow field is a function of time. First, the Navier-Stokes equations are transformed into computational space

$$\frac{1}{J}\frac{\partial U}{\partial \tau} + \frac{\partial E'}{\partial \xi} + \frac{\partial F'}{\partial \eta} + + \frac{\partial G'}{\partial \zeta} + \frac{\partial E'_v}{\partial \xi} + \frac{\partial F'_v}{\partial \eta} + \frac{\partial G'_v}{\partial \zeta} + U\frac{\partial(1/J)}{\partial \tau} = 0 \tag{10}$$

where J is the Jacobian of the coordinate transformation and (ξ, η, ζ) are the transformed computational coordinates in the streamwise, radial, and azimuthal directions of the cone. A seven point stencil is used to discretize the spatial derivatives

$$\frac{\partial f_i}{\partial x} = \frac{1}{hb_i}\sum_{k=-3}^{3}\alpha_{i+k}f_{i+k} - \frac{\alpha}{6!b_i}h^5\left(\frac{\partial f^6}{\partial^6 x}\right) \tag{11}$$

where the coefficients α and b are defined as

$$\alpha_{i\pm3} = \pm1 + \frac{1}{12}\alpha, \qquad\qquad \alpha_{i\pm2} = \mp9 - \frac{1}{2}\alpha$$

$$\alpha_{i\pm1} = \pm45 + \frac{5}{4}\alpha, \qquad\qquad \alpha_i = -\frac{5}{3}\alpha$$

$$b_i = 60$$

Here, h is the step size, $\alpha < 0$ is a fifth order upwind explicit scheme, and $\alpha = 0$ reduces to a sixth order central scheme. In this study the inviscid terms use $\alpha = -6$ which yields a low dissipation fifth order upwinded difference, and the viscous terms are discretized using $\alpha = 0$. The derivatives in the azimuthal direction are treated with Fourier collocation. To compute second derivatives, the first order derivative operator is applied twice. Flux splitting is applied with a local Lax-Friedrichs formulation. Additional details of the numerical methods of this study can be found in Zhong.[34]

In the shock-fitting formulation the shock itself is treated as a computational boundary at

$$\eta(x, y, z, t) = \eta_{max} = constant \tag{12}$$

and flow conditions behind the shock are calculated from Rankine-Hugoniot relations and a characteristic compatibility equation from the flow behind the shock. Additionally, the position $H(\xi, \zeta, \tau)$ and velocity $H_\tau(\xi, \zeta, \tau)$ of the bow shock in computational coordinates are also concurrently solved as independent flow variables using high-order finite difference. The details of this shock-fitting method can also be found in Zhong.[34] Finally, the simulations are advanced in time using Euler's method (RK-1) for computational speed.

B. LST

LST is commonly used to study the linear growth stage of the transition process, and tracks the growth of a disturbance that is governed by the linearized Navier-Stokes equations.[15] The LST equations are derived from the governing equations (Equation 1) where the instantaneous flow can be decomposed into a mean and fluctuating component $q = \bar{q} + q'$. Here q denotes flow variables such as velocity, pressure, temperature, etc. This instantaneous flow is then reintroduced into the governing equations. Since the steady mean flow is assumed to satisfy the governing equations it can be subtracted out. Furthermore, the mean flow is assumed to be a function of y only i.e. $\bar{q}(x, y, z) = \bar{q}(y)$ and the flow disturbances are assumed to be small enough such that higher order perturbation can be cancelled out. This assumption allows for the linearization of the equations. The perturbations are then assumed to be in the form of a normal mode described by

American Institute of Aeronautics and Astronautics

$q' = \hat{q}(y) \exp\left[i\left(\alpha x + \beta z - \omega t\right)\right]$, where ω is the circular frequency of the disturbance and α and β are the wavenumbers. In this study a spatial stability approach is used. Thus α is complex and results in the dispersion relation $\alpha = \Omega(\omega, \beta)$. For the spatial stability approach, the circular frequency of a disturbance mode, ω, must be manually set to be a real number, based on the disturbance frequency being studied, and the complex spatial wavenumber α can be written as $\alpha = \alpha_r + i\alpha_i$. Here, $-\alpha_i$ is the growth rate of the disturbance. Substituting in the normal mode form for the perturbation reduces the problem to a coupled set of 5 ordinary differential equations

$$\left(\mathbf{A}\frac{d^2}{dy^2} + \mathbf{B}\frac{d}{dy} + \mathbf{C}\right)\vec{\phi} = \vec{0}. \tag{13}$$

where $\vec{\phi} = \left[\hat{u}, \hat{v}, \hat{P}, \hat{T}, \hat{w}\right]^T$ and $\mathbf{A}$, $\mathbf{B}$ and $\mathbf{C}$ are complex square matrices of size 5. This is now a boundary value problem where the derivative operators can be discretized and the equations solved numerically. The system of equations is solved using using a multi-domain spectral based on Malik.[35] This was implemented and validated for a perfect gas flow over a circular cone by Lei and Zhong.[17]

LST gives information about what disturbance frequencies are unstable and the corresponding growth rates of those frequencies, but there is no information on the amplitude of the incoming disturbance. To estimate boundary-layer transition using LST, the e^N transition criterion is used which is defined as:

$$e^N = \frac{A(s)}{A_0} = \exp\left[\int_{s_0}^{s} -\alpha_i(s, f)ds\right] \tag{14}$$

where $A(s)$ is the integrated disturbance amplitude, A_0 is the initial disturbance amplitude, s_0 is the location where the disturbance first becomes unstable at the branch I neutral point, and α_i is the spatial amplification rate obtained from LST. The integration is performed for a constant frequency f, and is done numerically using trapezoidal integration. Note that a negative imaginary the wave number α results in disturbance growth while a positive value results in disturbance decay. The N-factor is specifically the exponent of e^N. In-flight transition N-factors are commonly understood to be between 5 and 10. However, this transition N-factor seems to hold only for sharp cones. Lei[17] and Aleksandrova et al.[36] found that N factors decreased considerably at similar streamwise locations for blunter cones, while Marineau[33] found that blunt nose N factors calculated at the beginning of transition were significantly lower than those for sharp nose cases, reaching as low as 0.5.

C.   Freestream Disturbance Model

The stability of the flow can also be studied by perturbing the meanflow and tracking the development of the resulting disturbances. Here, the flow is perturbed with freestream hotspot, fast acoustic, and slow acoustic disturbances in the form of Gaussian pulses. Freestream acoustic disturbances have been widely studied and can effectively introduce 2nd mode instability waves into flows about cones.[10–12, 16] In these prior studies, freestream acoustic disturbances were modeled with discrete Fourier modes. While this does allow for the simulations to approximate the continuously radiating disturbances found in experiments, the discrete nature of the equations makes it difficult to capture the broadband frequency spectrum of noise found in windtunnel and flight environments. Balakumar and Chou[11] attempted to model broadband freestream disturbances by combining discrete fourier mode disturbances into wave packets. While this does approximate broadband frequency disturbance behavior, this treatment still relies heavily on a manual selection of the necessary frequency bin size and the impinging acoustic mode amplitudes. On the other hand, Huang[20] implemented a freestream entropy spot (hotspot) disturbance modelled as a Gaussian pulse and found that these hotspot disturbances can excite strong acoustic modes in the boundary layer that continue to propagate downstream, eventually becoming the amplified 2nd mode. This shows that such a pulse model could be used to approximate continuous and broadband frequency freestream disturbances, and study the development of 2nd mode instabilities in cone geometries. The disturbances used in this study build upon the original work by Huang.[21] We first begin with the entropy spot disturbance given in Equation 15.

$$T(x, y, z, t) = \epsilon\, T_\infty exp\left(-\frac{R_c^2}{2\sigma^2}\right) + T_\infty \tag{15}$$

where the Gaussian parameters are given in Table 2.

Table 2. Gaussian pulse parameters for DNS.

| Pulse Geometry	ϵ	σ	x_0
Axisymmetric	$5E-4$	$1E-3$	$-0.02m$
Planar	$1E-6$	$1E-3$	$-0.02m$

Here, ϵT_∞ refers to the maximum freestream temperature perturbation amplitude. This amplitude was chosen to ensure that disturbances remained small enough to be applicable to remain in the linear growth regime.[4, 20] The term σ controls the width of the pulse and also determines the frequency content of the disturbance. The term R_c refers to the radial distance from the entropy spot to a point (x, y, z) in the flow field.

$$R_c = \sqrt{(x - x_{spot})^2 + (y - y_{spot})^2 + (z - z_{spot})^2} \tag{16}$$

In Eq. 16 the coordinates $(x_{spot}, y_{spot}, z_{spot})$ correspond to the center of the hotspot. We assume that the hotspot propagates purely in the streamwise direction such that $y_{spot} = z_{spot} = 0$ and $x_{spot} = x_0 + u_\infty t$ where x_0 is the initial location of the hotspot in the unsteady simulation. For a perfect gas the equation of state can be used to show that the resulting perturbed freestream density is

$$\rho(x, y, z, t) = \frac{p_\infty}{RT} \tag{17}$$

The parameters given in Table 2 for the axisymmetric cases result in the pulse shown in Figure 2.This model for the freestream hotspot perturbation allows for potentially more complex freestream disturbances, as the shape, incidence location, and intensity of the disturbance can be tuned accordingly. The cases presented here were perturbed with uniform axisymmetric and planar disturbances propagating along the center-line of the cone, using the parameters in Table 2 where the pulse width parameter σ was chosen to encompass significant freestream disturbances at frequencies up to 600 kHz, as shown in Marineau's study.[33] The spectral distribution (in frequency) of the planar disturbances followed the same trends as the axisymmetric cases, with the only difference being in the reduction of the peak disturbance amplitude. The amplitude of the planar disturbances were reduced so as to ensure that the downstream perturbations remained linear, as the planar disturbances caused shock-disturbance interactions along the entire length of the cone.
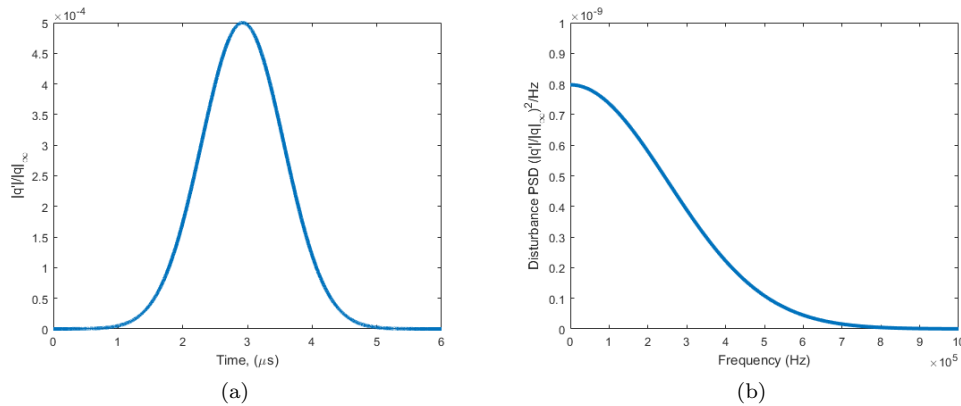
Figure 2. Freestream disturbance distributed over (a) time and (b) frequency for axisymmetric pulse.

The acoustic freestream disturbances were also modelled using the same Gaussian model. A simple planar acoustic disturbance assumes a disturbance amplitude distribution in the form of Eq. 18.

$$q(x, y, z, t) = |q'|_\infty exp\left(-\frac{(x - C_\infty)^2}{2\sigma^2}\right) + q_\infty \tag{18}$$

American Institute of Aeronautics and Astronautics

For acoustic disturbances, the coefficient q corresponds to any perturbed variable in the freestream. Additionally, q' represents the perturbation amplitude of each of these variables normalized by the freestream value. In the case of a fast acoustic disturbance, the freestream disturbance amplitudes follow the dispersion relations given by:

$$|\rho'|_\infty = \frac{|P'|_\infty}{\gamma} = |u'|_\infty M_\infty \quad |s'|_\infty = |v'|_\infty = |w'|_\infty = 0 \tag{19}$$

A slow acoustic disturbance in the freestream is governed by a very similar dispersion relation:

$$|\rho'|_\infty = \frac{|P'|_\infty}{\gamma} = -|u'|_\infty M_\infty = \epsilon M_\infty \quad |s'|_\infty = |v'|_\infty = |w'|_\infty = 0 \tag{20}$$

Furthermore, these acoustic disturbances propagate in the freestream at a phase speed of C_∞, which is defined as

$$C_\infty = u_\infty \pm a_\infty \tag{21}$$

for fast(+) and slow(-) acoustic waves respectively. In equation 21 u_∞ is the freestream velocity and a_∞ is the speed of sound. The axisymmetric acoustic pulse is defined in a similar manner in Eq. 22.

$$q(x, y, z, t) = |q'|_\infty exp\left(-\frac{(R_{ac})^2}{2\sigma^2}\right) + q_\infty \tag{22}$$

The variables and disturbance amplitudes here are the same as those for the 1-D convected pulse, with the exception of the R_{ac} term. Similar to the axisymmetric pulse, this variable is given by the expression:

$$R_{ac} = \sqrt{(x - x_{pulse})^2 + (y - y_{pulse})^2 + (z - z_{pulse})^2} \tag{23}$$

In this case the pulse was centered along the cone, requiring $y_{pulse} = z_{pulse} = 0$, while being convected downstream through the term

$$x_{pulse} = x_0 + C_\infty t \tag{24}$$

Again, x_0 corresponds to the initial x position of the pulse which is set during the beginning of the simulation.

D. Boundary Layer Receptivity

The pulse disturbances imposed onto the cone in the unsteady simulations were chosen to induce broadband frequency perturbations in the boundary layer of the cone. LST was used to validate the results of the unsteady DNS analysis, which requires decomposing the disturbances into individual frequency components. For an unsteady, time-dependent disturbance a temporal Fourier spectral analysis was used on the boundary layer perturbations.

The time-dependent perturbation variables can be expressed in terms of their Fourier spectral components, obtained through FFT:

$$h(t_k) \equiv h_k \approx \sum_{n=0}^{N-1} H(F_n) e^{-2\pi i F_n t_k} \tag{25}$$

where $H(F_n)$ is the frequency space Fourier coefficient corresponding to the nth discretized frequency F_n. Additionally, N corresponds to the total number of Fourier collocation points used to discretize the time-dependent function $h(t)$ in Fourier space. The discretized time function h_k is defined as being the value of the function $h(t)$ at a given time $t = t_k$.

In this study, the variable $h(t)$ corresponds to local boundary-layer perturbations in flow variables such as pressure, velocity, density, and temperature. The complex Fourier coefficients $H(F_n)$ correspond to the frequency space distribution of these perturbation variables, and $|H(F_n)|$ are the perturbation amplitudes for these variables at a given frequency.

Since LST was used to validate the results of the unsteady DNS analysis, local growth rates and wavenumbers need to be calculated from the Fourier decomposed perturbation data. Following Mack,[15] the local growth rates for each frequency are determined by

$$-\alpha_i = \frac{1}{|H(F_n)|}\frac{d|H(F_n)|}{ds} \tag{26}$$

American Institute of Aeronautics and Astronautics

and the local wave numbers are determined by

$$\alpha_r = \frac{d\psi_n}{ds} \tag{27}$$

where s corresponds to the local streamwise coordinates and ψ_n is phase angle of the nth frequency. The phase speed of a given disturbance at a given frequency is defined as

$$c_r = \frac{2\pi F_n}{\alpha_r} \tag{28}$$

The response of the system to each freestream disturbance environment is can be represented through a receptivity coefficient. This receptivity coefficient, defined here as the initial amplitude of the 2nd mode disturbance $A_0(f) = C_{rec}(f)$, is found by

$$A_0(f) = C_{rec}(f) = \frac{A(f)}{e^{N(f)}} \tag{29}$$

where $A(f)$ is the normalized fourier decomposed pressure disturbance at a given frequency and $e^N(f)$ is the amplification factor (N-factor) determined through LST analysis for a given frequency f. The streamwise sampling locations of both the N-factor data and the unsteady pressure perturbation data are the same in order to isolate the initial amplitude of the 2nd mode disturbance. By doing so, the multimodal nature of the boundary layer disturbances can be removed. Thus, the spectrum of receptivity coefficients for linear 2nd mode growth can be produced using a combination of LST and unsteady DNS data. We see later that the choice of sampling location does have some influence on the resulting receptivity coefficients by this definition.

V.   Steady Flow Field Solution

The steady DNS pressure and mach number contours for the cone are shown in Figure 3 for the first zone at the nose, and the second zone at the beginning of the cone frustum. Figure 4 presents the grids used at this location. A total of 240 points were used in the η direction, while the distribution in the ξ ranged from 30 points per mm at the nose to 5 points per mm at the end of the geometry. These distributions were chosen to esnure that sufficiently low wavenumber disturbances could be captured by the simulation and to provide sufficient resolution in the meanflow data so as to reduce numerical inconsistencies in the LST analysis. A total of 10,080 points were used in the ξ direction to resolve the cone to 1.9 m.
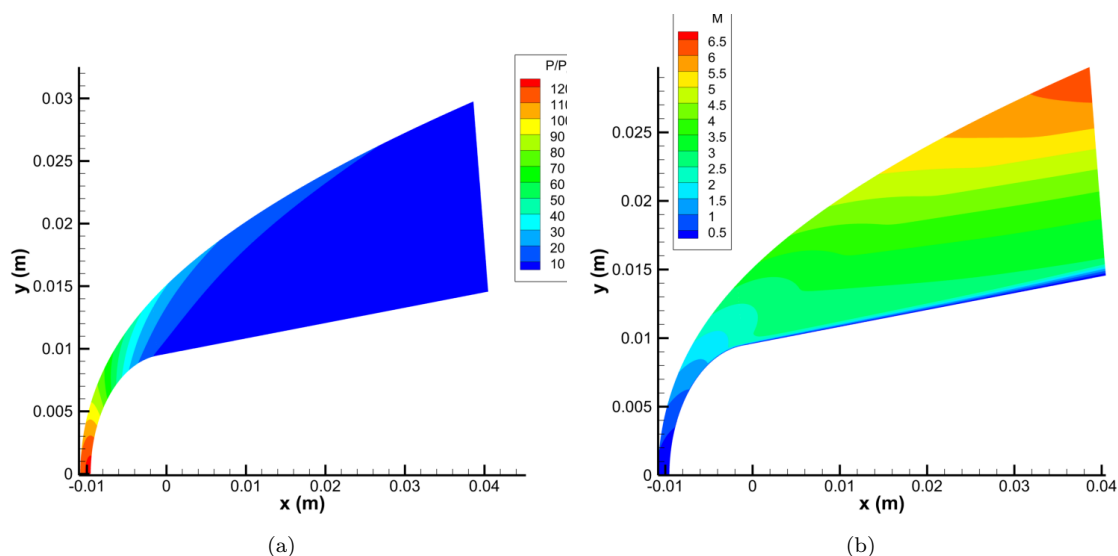

Figure 3.   Partial view of meanflow (a) pressure and (b) mach number for zones 1 and 2 near nose region.

American Institute of Aeronautics and Astronautics

Similar pressure and mach number contours for the full cone are shown in Figure 5. The mach number contours in Figure 3b and Figure 5b show evidence of a moderate entropy layer extending to approximately $x = 0.4m$ as a band of relatively low Mach numbers behind the shock. These entropy layers reduce local flow velocities, and in turn reduce local Reynolds numbers. Since transition locations have been correlated with larger local Reynolds numbers, this process has been used to explain the transition delaying mechanism for intermediate nose bluntness.[37] However, this fails to explain transition reversal effects observed in large bluntness flows.[17] Zhong and Ma[16] also showed the emergence of an additional generalized inflection point due to the entropy layer as a possible outcome, along with non-modal disturbance growth. Further investigation of the effects of freestream receptivity in the entropy layer may be of interest in resolving this problem.

Marineau[33] studied cones up to lengths of 1.5m. The domain here was lengthened to study the further downstream development of disturbances excited by the freestream pulses considered in this work, and to determine if a significant supersonic mode could be observed in this low enthalpy case. The steady solution for this case was then used to study the development of boundary layer disturbances through both LST and unsteady DNS analysis.
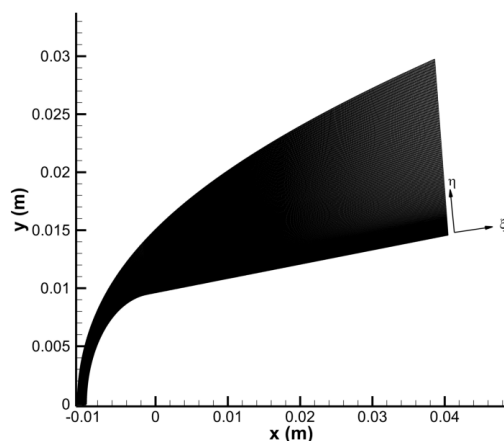
Figure 4. Partial view of grid distribution for zones 1 and 2 near nose region.

(a)

(b)
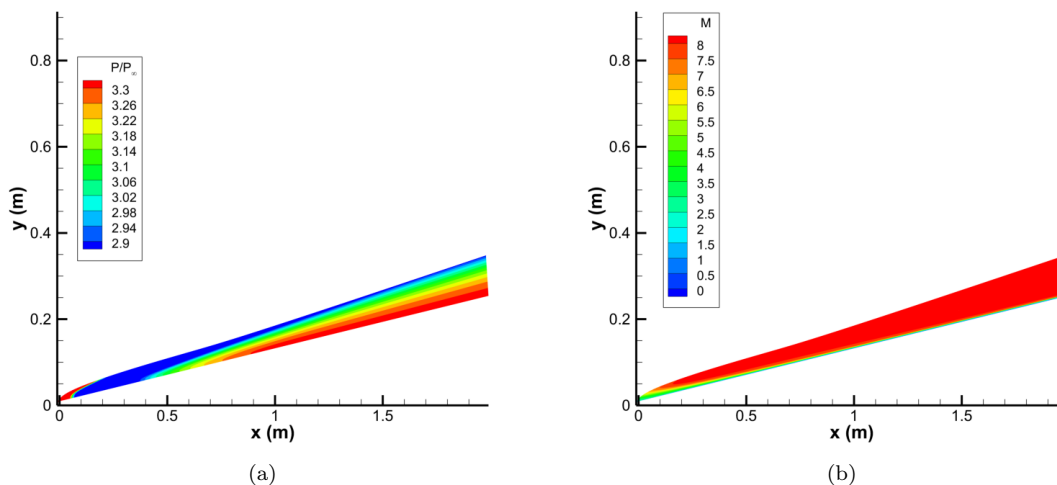
Figure 5. Meanflow (a) pressure and (b) mach number for entire cone.

American Institute of Aeronautics and Astronautics

VI.   LST Results

LST results have indicated an strong amplified 2nd mode band between frequencies of 118 kHz and 238 kHz. At the reported experimental transition location of 1.037m for this case,[33] the unstable 2nd mode is found between frequencies of 150 and 185 kHz. This compares well to Marineau's results. The growth rate contours are shown in Figure 6a and the neutral curve is shown in Figure 6b. The negative growth rates in Figure 6a are the unstable frequencies and the neutral curve was generated by fitting the branch I and branch II neutral stability points shown in Figure 6a.

(a)

(b)
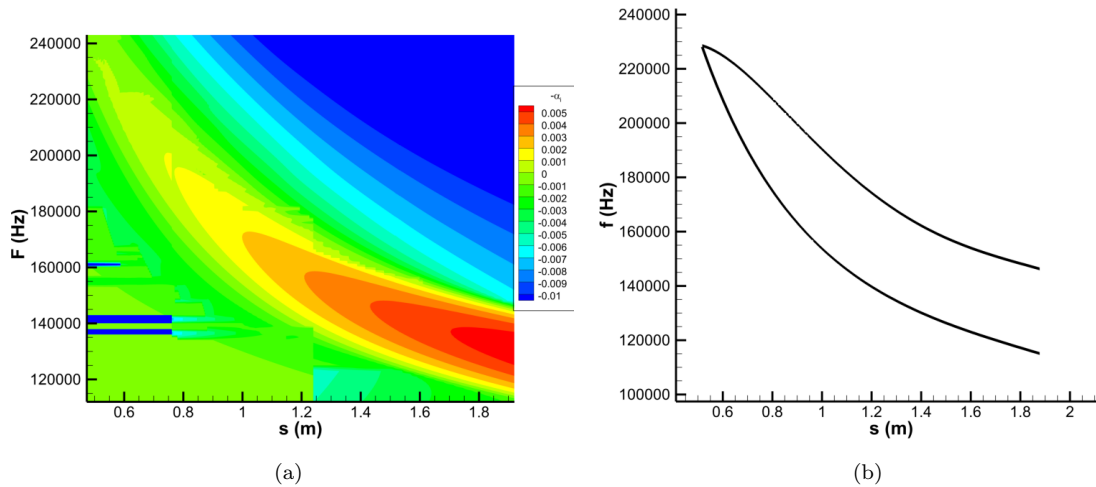
Figure 6. LST results (a) Growth Rate Contour (b) Neutral Curve

For discrete frequencies, an N factor can be calculated using Equation 14. Given the experimentally determined transition locations from Marineau,[33] transition N-factors and their associated peak frequencies can be obtained. Figure 7a presents N-factor curves for frequencies ranging from 120 to 240 kHz.

(a)

(b)
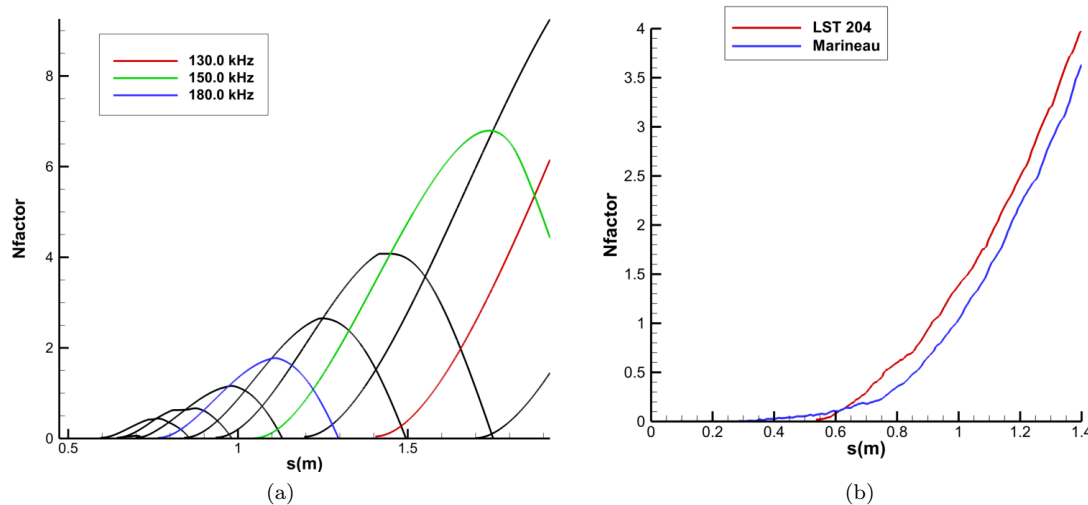
Figure 7. (a) N-factor data ranging between 120 kHz to 220 kHz with $\Delta f = 10$ kHz. (b) Current LST N-factors vs. Marineau's[33] reported PSE N-factors.

For this case (which corresponds to Run 3752), Marineau[33] reported an experimentally determined transition location of $s = 1.037m$, along with a corresponding N factor of 1.6. A direct comparison between

American Institute of Aeronautics and Astronautics

the fitted profile of the LST N-factors in Figure 7a and Marineau's PSE derived N-factors are shown in Figure 7b, which was made by fitting the curve profiles for each of the sampled LST frequencies. Our LST reports a peak disturbance frequency of 176 kHz at the experimental transition location, with an N-factor of approximately 1.7. This is consistent with Marineau's reported results for this case. In general, the LST results correlate reasonably well with those reported by Marineau, with our LST overpredicting the N-factors slightly throughout the downstream sections of the domain. This difference can be attributed to non-parallel effects that the LST formulation neglects compared to the PSE package utilized by Marineau.

Several of the higher frequency N-factor curves in Figure 7a show some deviation from the expected smooth Nfactor shape. This is indicative of discontinuities in the growth rate, and may attributed to either numerical resolution issues in the LST solution algorithm or interaction with additional disturbance modes that were not captured in the current analysis. These can include additional discrete modes such as mode F2 originating from the fast acoustic spectrum.

(a) (b)
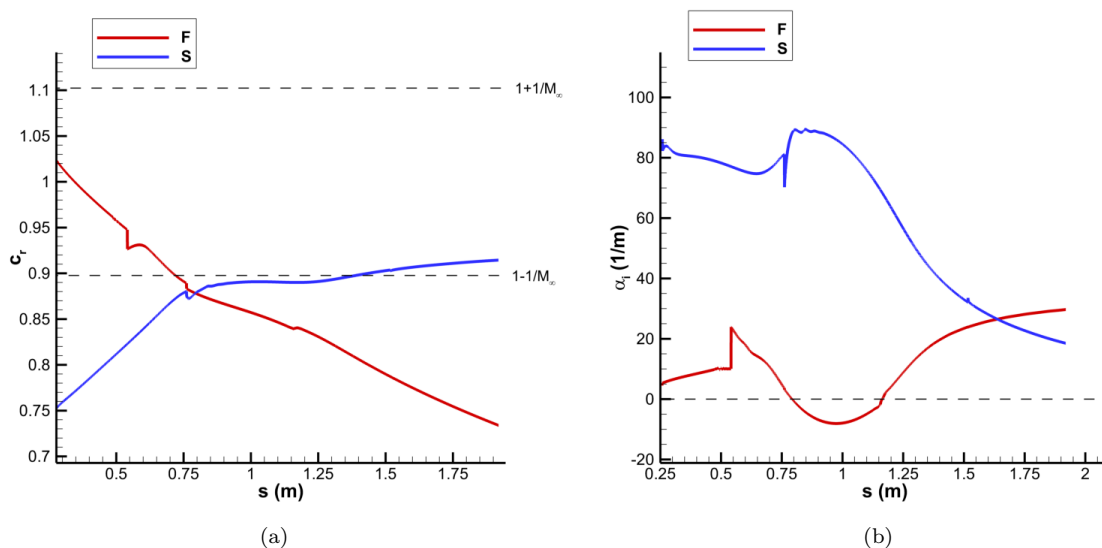
Figure 8. Streamwise LST results at f = 176 kHz for (a) Phase Speed (b) Growth Rate.

(a) (b)
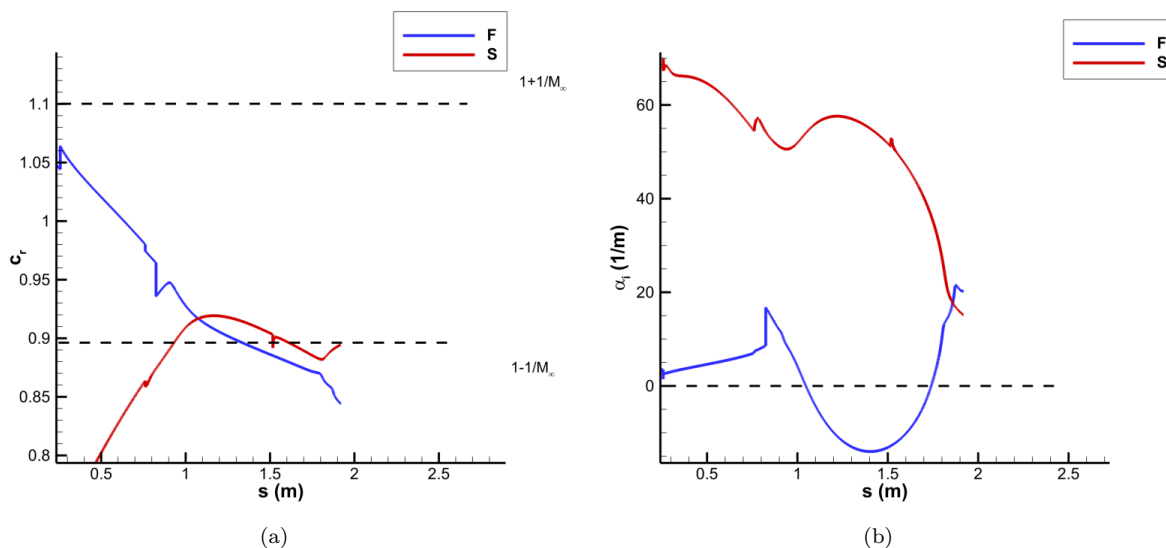
Figure 9. Streamwise LST results at f = 150 kHz for (a) Phase Speed (b) Growth Rate.

American Institute of Aeronautics and Astronautics

The streamwise LST results for the case are also presented in Figure 8 for the 176 kHz disturbance. From Figure 8a and Figure 8b it is apparent that the unstable disturbance here originates from the fast acoustic spectrum and that Mode F corresponds to the unstable 2nd mode for this case. In addition, Figure 8b shows the disturbance being amplified between $s = 0.79$ m and $s = 1.22$ m for the 176 kHz case. The discontinuities in these figures can be attributed to the synchronization between Mode F and Mode S disturbances, which can be difficult to resolve numerically.[35]

An additional result is shown in Figure 9 for a 150 kHz disturbance, which is one of the most amplified frequencies predicted by LST near the end of the domain. Again, it is shown that the primary 2nd mode disturbance originates from the fast acoustic spectrum and is the mode F disturbance. Additionally, Figure 9 shows that this particular frequency demonstrates an extensive synchronization region between mode F and mode S, lying between 1.1 and 1.7 m along the cone. The discontinuity at $s = 0.75m$ in Figure 8b is due to synchronization. The discontinuities at $s = 0.5m$ and in Figure 8 and at $s = 0.8m$ in Figure 9 can be attributed to issues in the numerical resolution of the LST algorithm near synchronization.
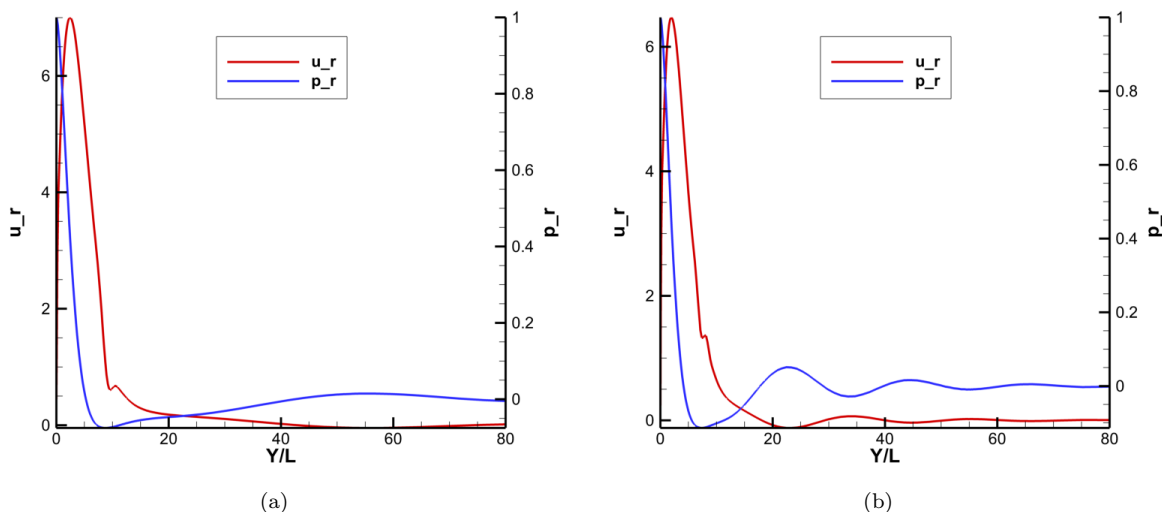
Figure 10. Velocity and pressure streamfunctions for the 176 kHz disturbance at (a) 1.037m and (b) 1.41m
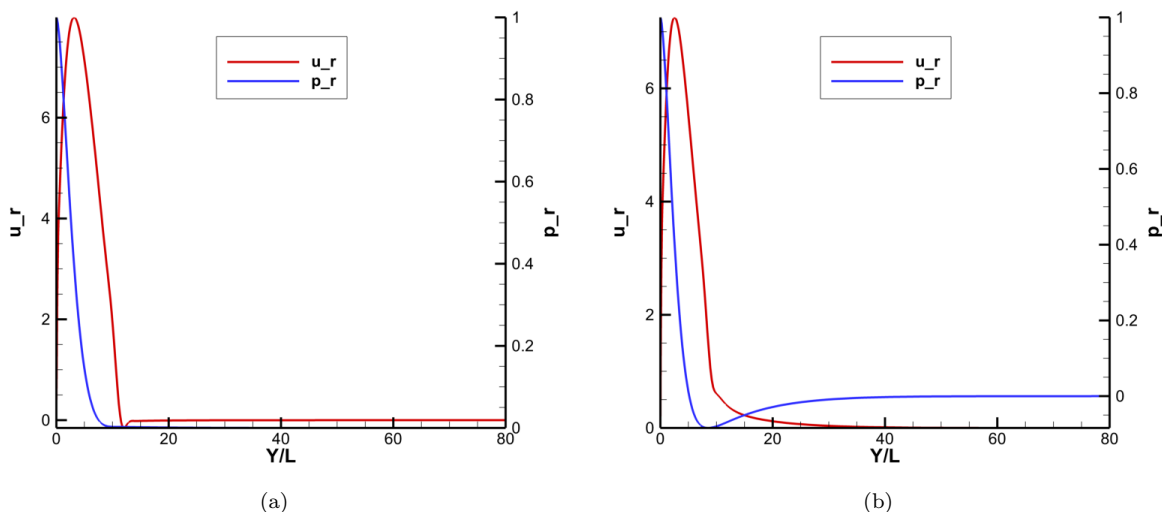

Figure 11. Velocity and pressure streamfunctions for the 150 kHz disturbance at (a) 1.037m and (b) 1.41m

American Institute of Aeronautics and Astronautics

The eigenfunctions for the unstable mode F are presented in Figure 10a and Figure 10b for the 176 kHz disturbance. Figure 10a shows the pressure and velocity eigenfunctions for the 176 kHz disturbance at the experimental transition location of $s = 1.037m$ while Figure 10b depicts the same results at $s = 1.41m$, which corresponds to the peak amplification point for the 150 kHz disturbance. Figure 11a and Figure 11b present the same results for the 150 kHz disturbance at $s = 1.037m$ and $s = 1.41m$ respectively.

The pressure eigenfunction curve in Figure 10a is indicative of a discrete mode F1 instability, containing one apparent peak and one apparent valley.[6] The same pressure eigenfunction at the downstream location in Figure 10b sees significant oscillations, which may be indicative of multimodal influences at this disturbance frequency. This is likely because the sampled location is outside of the unstable 2nd mode region for the 176 kHz disturbance, causing the LST algorithm to have difficulties latching onto a dominant mode. Figure 11a for $s = 1.037m$ and Figure 11b similarly depict the eigenfunctions of the unstable Mode F. Each of these results also show that the modes decay quickly after exiting the boundary layer, and depict strong 2nd mode eigenfunction shapes when the unstable mode is dominant.

VII.   Unsteady DNS Results and LST Comparison

The receptivity of the cone was studied in response to a variety of freestream pulse disturbances. First, the pulse was introduced upstream of the nose and then convected through the domain in a streamwise manner. The resulting boundary layer disturbances on the cone's surface were studied by using FFT to decompose the surface pressure perturbations into their spectral frequency components. The specific disturbance cases and their respective labels are given in Table 3. The disturbances are differentiated by both their freestream perturbation type and by their spatial extent. The fast acoustic, slow acoustic, and hotspot (entropy spot) disturbances are defined by their freestream dispersion relations discussed previously in Equations 18, 19, and 20. The axisymmetric pulses are finite in three dimensions, while the planar pulses are again semi-infinite in the y-z plane but finite along x. The frequency distribution of the pulses was chosen to be the same in each case.

Table 3.   Freestream flow conditions for DNS simulations.

Disturbance Type	Case
Axisymmetric Fast Acoustic	B1
Axisymmetric Slow Acoustic	B2
Axisymmetric Hotspot	B3
Planar Fast Acoustic	B4
Planar Slow Acoustic	B5

Figure 12 for the finite axisymmetric hotspot (Case B3) shows the pressure disturbance contours near the end of the cone after perturbation by an axisymmetric hotspot (Case B3). Similar results are observed for the other planar and axisymmetric disturbance cases as well. The rope-like wave structures shown here are indicative of a perturbation growing in accordance with Mack's 2nd mode.[4] Figure 13 similarly shows the pressure perturbation contours for the planar slow acoustic disturbance (Case B5) which show similar rope-like structures indicative of the 2nd mode.
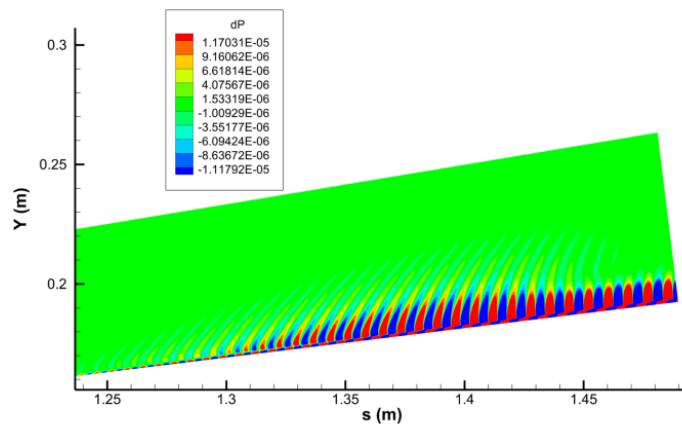
American Institute of Aeronautics and Astronautics

Figure 12. Pressure perturbations near s = 1.5 m after the finite axisymmetric hotspot perturbation (Case B3).

In addition to the conventional 2nd mode, mach wave-like radiating structures can be observed near the tail end of the disturbance wavepacket. This behavior is characteristic of a supersonic mode, in which the phase speed of the disturbance is supersonic with respect to the mean flow.[38] Recent studies have shown that these supersonic modes may have disturbance amplitudes similar in strength to the 2nd mode instabilities, and may be of significant importance in the process of transition.[38–41] Of particular note is that the supersonic mode observed here has occurred in a perfect gas case whereas Knisely[38–40] and Mortensen[41] observed significant supersonic modes in high-enthalpy flows with strong thermochemical nonequilibrium. This indicates that a significant supersonic mode may be present in a wider range of conditions than previously believed. While the downstream location of these supersonic modes makes it unlikely that they affect the transition behavior of this particular case, they may play a role in mechanisms such as nonlinear breakdown from finite amplitude disturbances that occur far downstream.
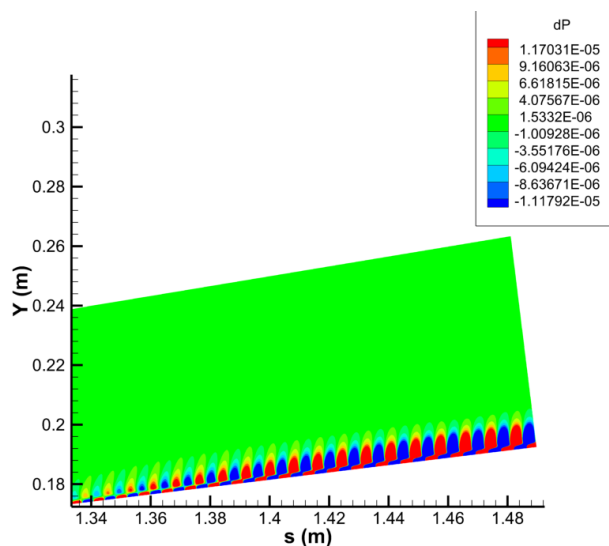
Figure 13. Pressure perturbations near s = 1.5 m after the planar slow acoustic perturbation (Case B5).

A. FFT Decomposed Pressure PSD

The total surface pressure perturbations along the downstream regions are presented in Figure 14 for the axisymmetric hotspot (Case B3). The disturbance wave packet is shown to decay upstream of the 2nd

American Institute of Aeronautics and Astronautics

mode region, before experiencing amplification. These surface disturbances can be decomposed into spectral frequency data using a FFT. The resulting normalized surface pressure power spectral density (PSD) contours for the axisymmetric fast acoustic (Case B1), slow acoustic (Case B2), and hotspot (Case B3) disturbances are shown in Figure 15. Additionally, the surface pressure PSD for the planar fast acoustic (Case B4) and slow acoustic (Case B5) disturbances are presented in Figure 16. These fourier decomposed pressure disturbances are normalized by the spectral content of the initial freestream disturbance in Figure 2b.
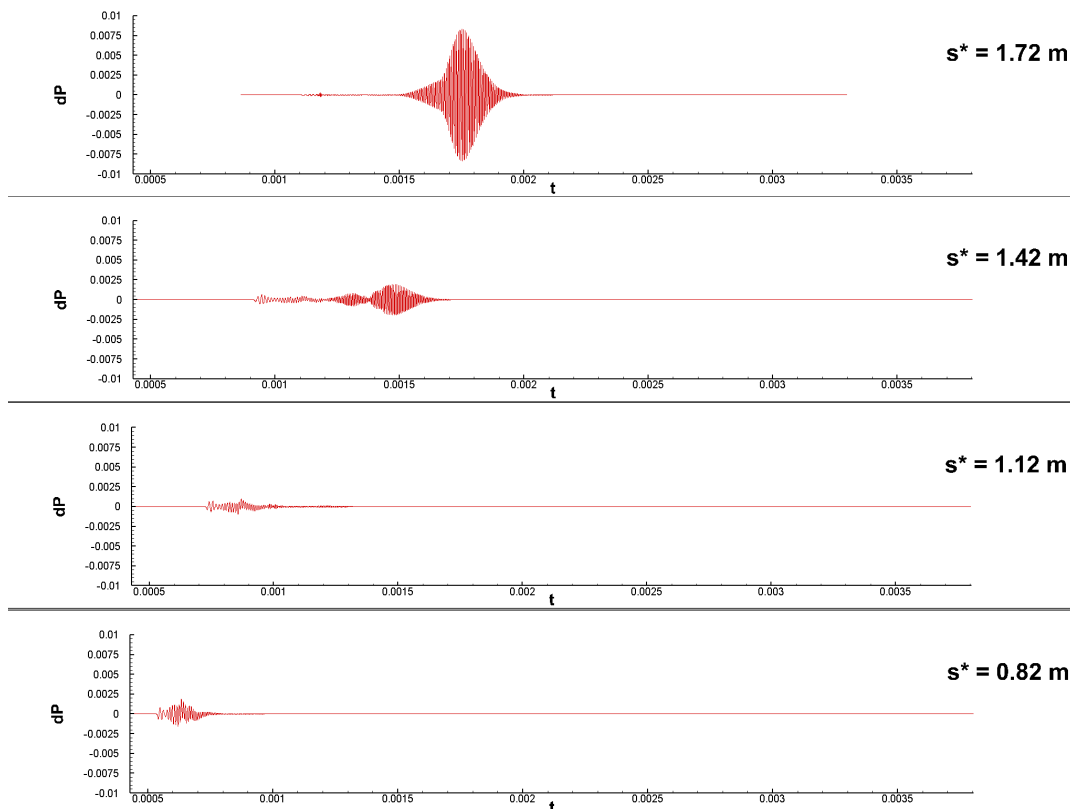
Figure 14. Time history of pressure perturbations in downstream region of Case 2 for an axisymmetric hotspot disturbance (Case B3).

Figure 15 shows that the three axisymmetric pulses similarly excite the 2nd mode in the downstream portions of the cone. An additional disturbance band between 100 kHz and 200 kHz is shown at the beginning of the domain and corresponds to the forcing waves generated by the shock-disturbance interaction upstream. This initial perturbation is attenuated until the 2nd mode region, where amplification begins. The initial forcing waves seem strongest for the axisymmetric fast acoustic disturbance (Case B1), followed by the hotspot (Case B3) and then the slow acoustic (Case B2) disturbances.

The PSDs for the planar acoustic pulses in Figure 16 show similar phenomena. In particular, Figure 16b for the planar slow acoustic pulse (Case B5) depicts a similar initial disturbance near the beginning of the plotted domain that is partially attenuated before 2nd mode amplification. However, an additional narrow disturbance band neighboring the 2nd mode here can be seen, and may be attributed to the continuous forcing provided by the planar disturbance front propagating through the domain. On the other hand, Figure 16a shows that while the planar fast acoustic disturbance (Case B4) also generates a 2nd mode disturbance band between 100 and 200 kHz in the upstream regions, the frequencies associated with the forcing seem to experience amplification instead of attenuation as they move downstream.
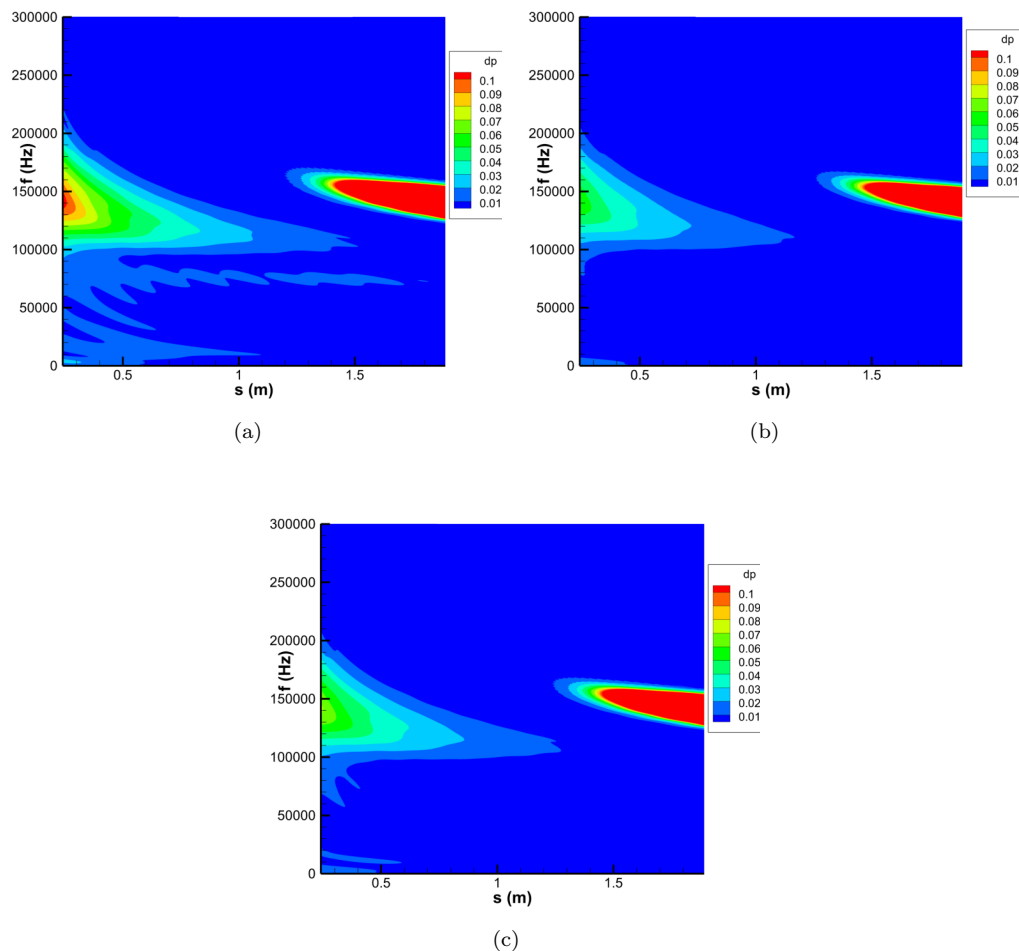
American Institute of Aeronautics and Astronautics

(a)

(b)

(c)

Figure 15. Surface FFT pressure distribution for (a) Case B1, (b) Case B2, and (c) Case B3.

(a)

(b)
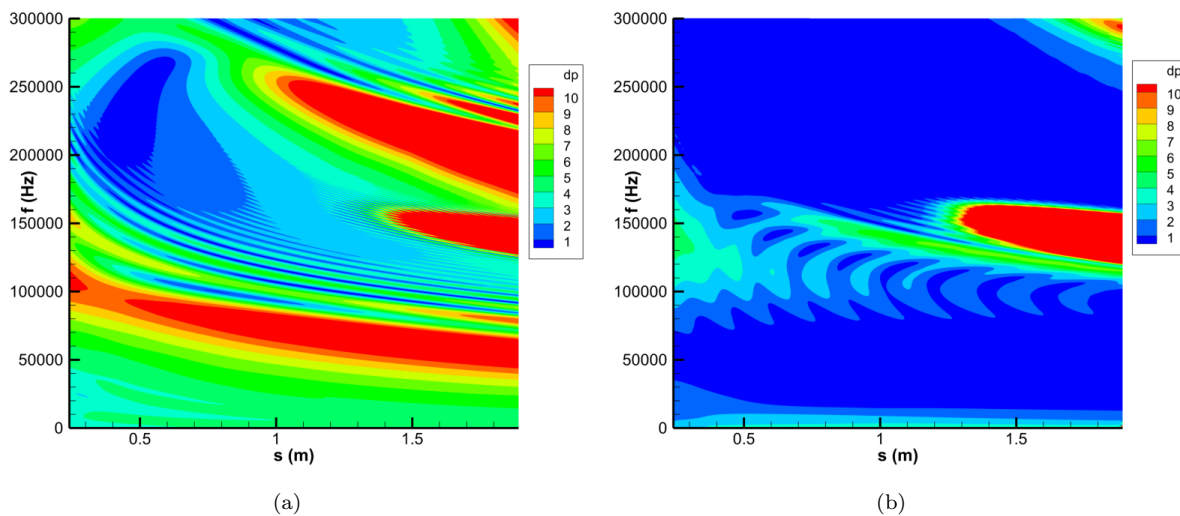
Figure 16. Surface FFT pressure distribution for (a) Case B4 and (b) Case B5.

American Institute of Aeronautics and Astronautics

Figure 16a for the planar fast acoustic (Case B4) pulse also shows an additional instability between 160 kHz and 260 kHz that isn't observed in the planar slow acoustic or any of the axisymmetric cases, indicating that Case B4 is able to much more readily excite a variety of instabilities in the boundary layer here. A rescaled contour plot for Case B4 in Figure 17 shows that the strongest disturbance is still associated with the 2nd mode. However, the strongest perturbation at the experimentally determined transition location of s = 1.037 m for this case does not lie within the 2nd mode frequency band. Instead, a lower frequency disturbance at 76 kHz and a higher frequency disturbance at 252 kHz both have perturbations five to six times stronger than those found in the 2nd mode region predicted by LST for this point. It is apparent that for Case B4, these other instability modes have significant effects on the receptivity response off the flow to the planar fast acoustic disturbance (Case B4) both at the experimentally determined transition location and downstream on the cone.
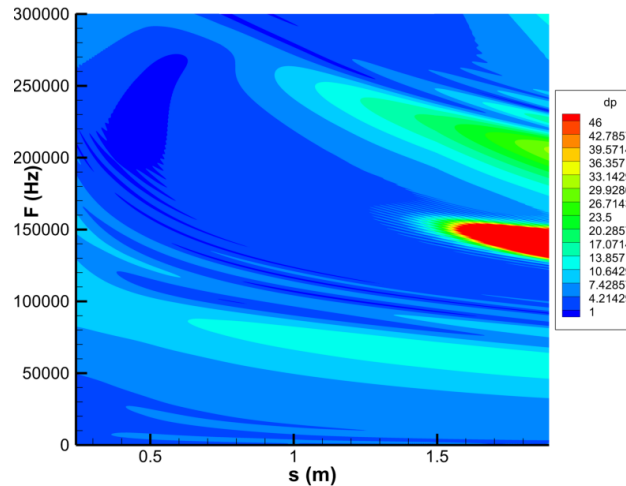

Figure 17. Rescaled FFT contours of surface pressure perturbations for Case B4.

A further comparison can be made by comparing these PSD contours with the neutral stability curve derived from LST. The resulting comparison figures are shown in Figure 18 for Cases B1 through B3 and Figure 19 for Cases B4 and B5. From Figure 18 and Figure 19 it can be seen that there is an extensive frequency band of disturbances contained between 135 to 175 kHz centered around the branch II neutral point in the downstream portion of the cone in each of the five disturbance cases. This indicates a strong amplification of 2nd mode disturbances at these downstream locations.

American Institute of Aeronautics and Astronautics

(a)

(b)

(c)
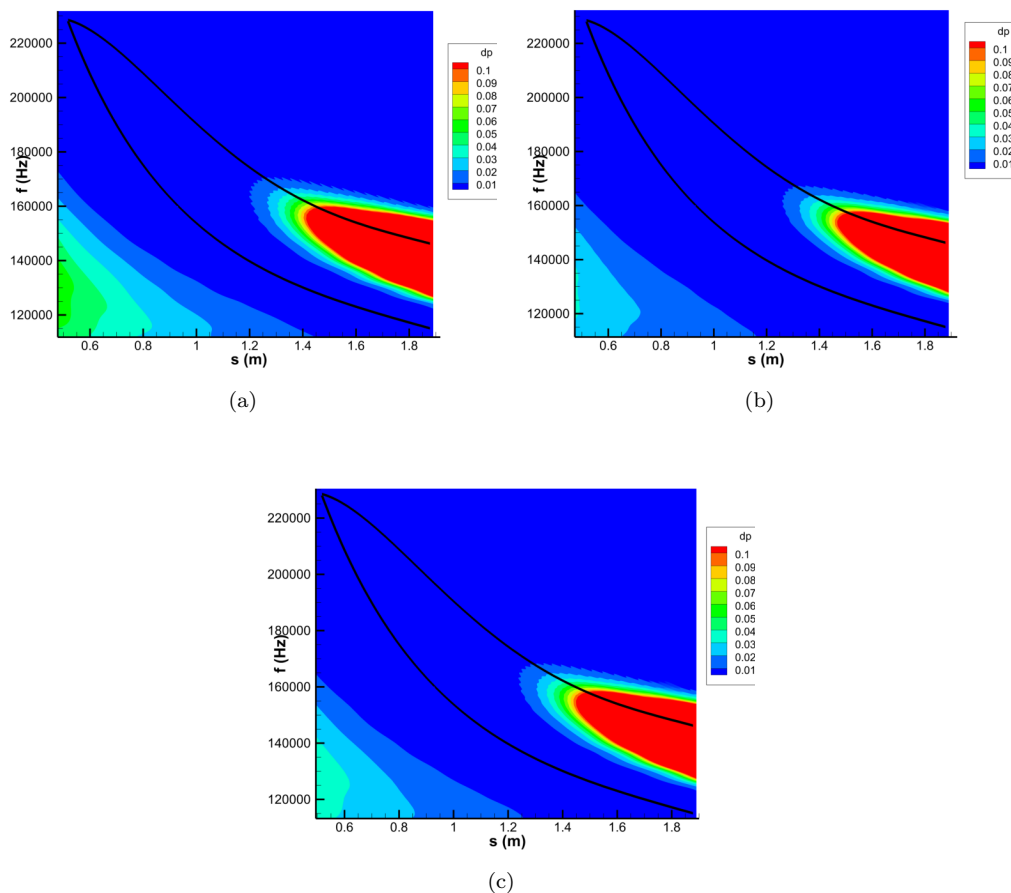
Figure 18. Surface FFT pressure distribution vs. LST neutral curve for (a) Case B1, (b) Case B2, and (c) Case B3.

Additionally, while N-factor amplification is typically calculated through integrating LST-derived growth rates, they can also be extracted directly from the unsteady results. Equation 14 defines the N-factor both through an integrated LST growth rate, as well as the ratio between an arbitrary location and the initial disturbance amplitude in the 2nd mode region. Using the latter definition, the N-factors can also be extracted from the unsteady DNS results. The DNS-derived N-factor contours are presented in Figure 20 for the axisymmetric and planar fast acoustic disturbance cases (Case B2 and Case B4).These unsteady N-factor contours are very similar to the FFT decomposed surface pressure distributions shown in Figures 15 through 19. The primary instabilities in the unstable 2nd mode region still experience the strongest downstream amplification in frequencies ranging between 140 kHz to 150 kHz. It was found that Case B2's results shown in Figure 20a correlated very well with the LST results in Figure 7a. The peak N-factor from LST at the end of the domain was found to be approximately 9.21, while the DNS results showed a maximum N-factor of 9.11. The results for Case B4 showed a significantly smaller peak amplification of 6.54 at the same location and frequency. This can be explained by the modulation of the initial 2nd mode waves in the planar acoustic case due to the additional forcing from the extended shock-disturbance interactions seen in the planar disturbance cases. These additional disturbances can significantly increase the perturbation levels at the branch I neutral point that are used to normalize other disturbances in the plotted region.
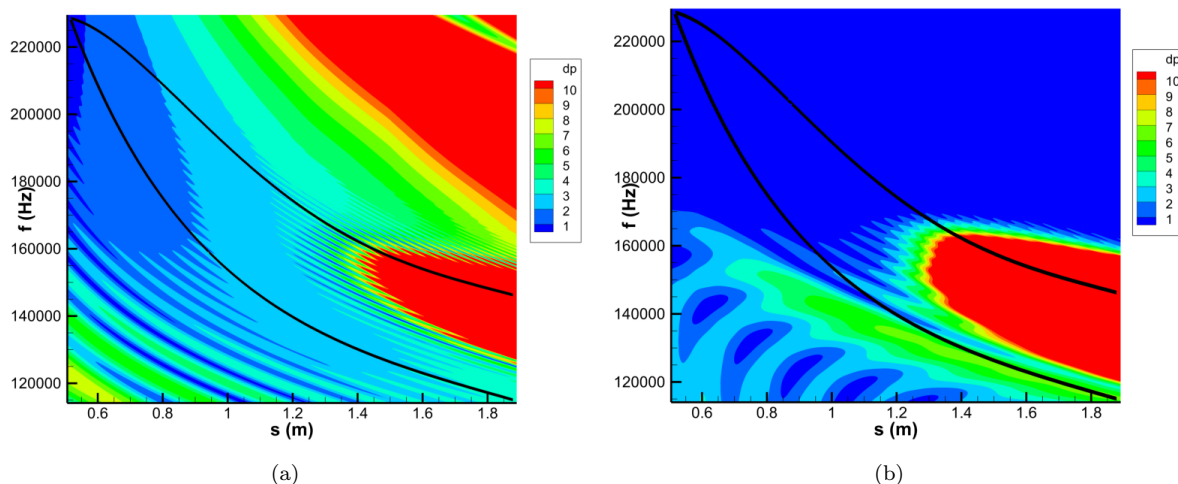
Figure 19. Surface FFT pressure distribution vs. LST neutral curve for (a) Case B4 (b) Case B5.
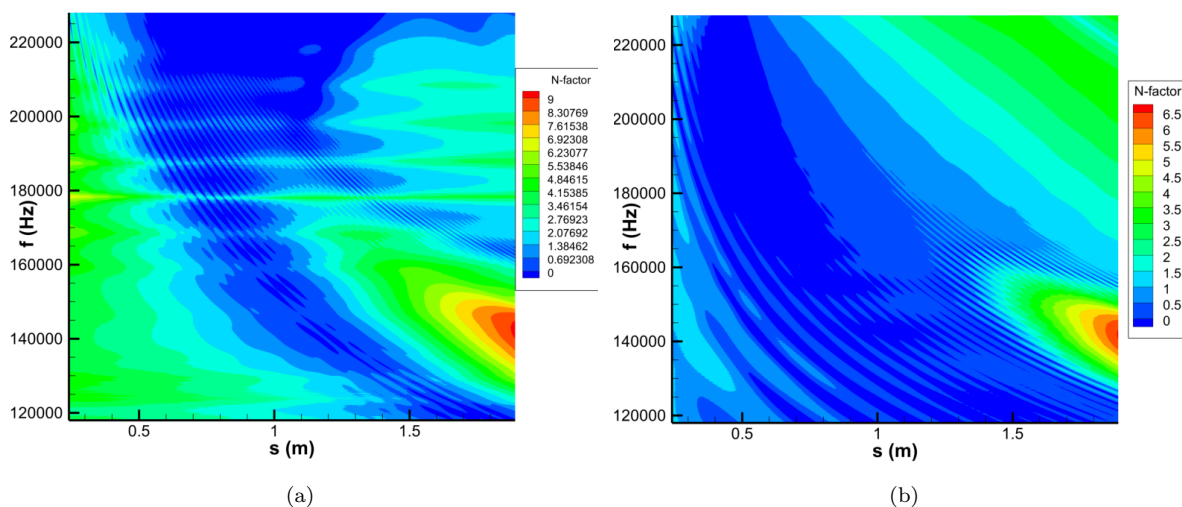

Figure 20. Unsteady DNS-derived N-factor contours for (a) Case B1 and (b) Case B4.

The FFT decomposed surface pressure perturbations at different streamwise locations are also presented in Figure 21 for cases B1 through B3 and Figure 22 for cases B4 and B5. The spectra of the surface pressure perturbations are plotted at several locations both upstream and downstream of the 2nd mode amplification region. As expected, the spectral surface pressure distributions for the axisymmetric cases are very similar to each other. Again, we see that Case B1 excites the strongest overall pressure perturbations downstream in the 2nd mode region. Case B1 also generates stronger initial disturbance waves upstream of the 2nd mode amplification region as observed the PSD contours. Distinctive peaks in the disturbance amplitude can also be seen here, initially centered around frequencies of approximately 170-180 kHz. As we move further downstream this peak disturbance band shifts to center around lower frequencies while also growing in overall amplitude. This peak eventually centeres around 145-150 kHz near the end of the computational domain. The amplitude peaks observed here correspond to the primary 2nd mode instability for this flow. This shift to lower frequencies in the downstream regions can also be seen in the LST results in Figure 6, as optimal disturbances are expected to follow with the branch II neutral point. Additionally, the disturbance

American Institute of Aeronautics and Astronautics

spectra at the earlier sampling locations show much smaller peaks near the second mode frequencies that dampen as they move downstream. These are seen to begin amplifying again after $s = 0.915m$ and confirms the initial decay and eventual amplification of 2nd mode instabilities expected for this cone geometry. While the spectral amplitudes for Cases B2 and B3 are smaller, the same general trends are observed there.
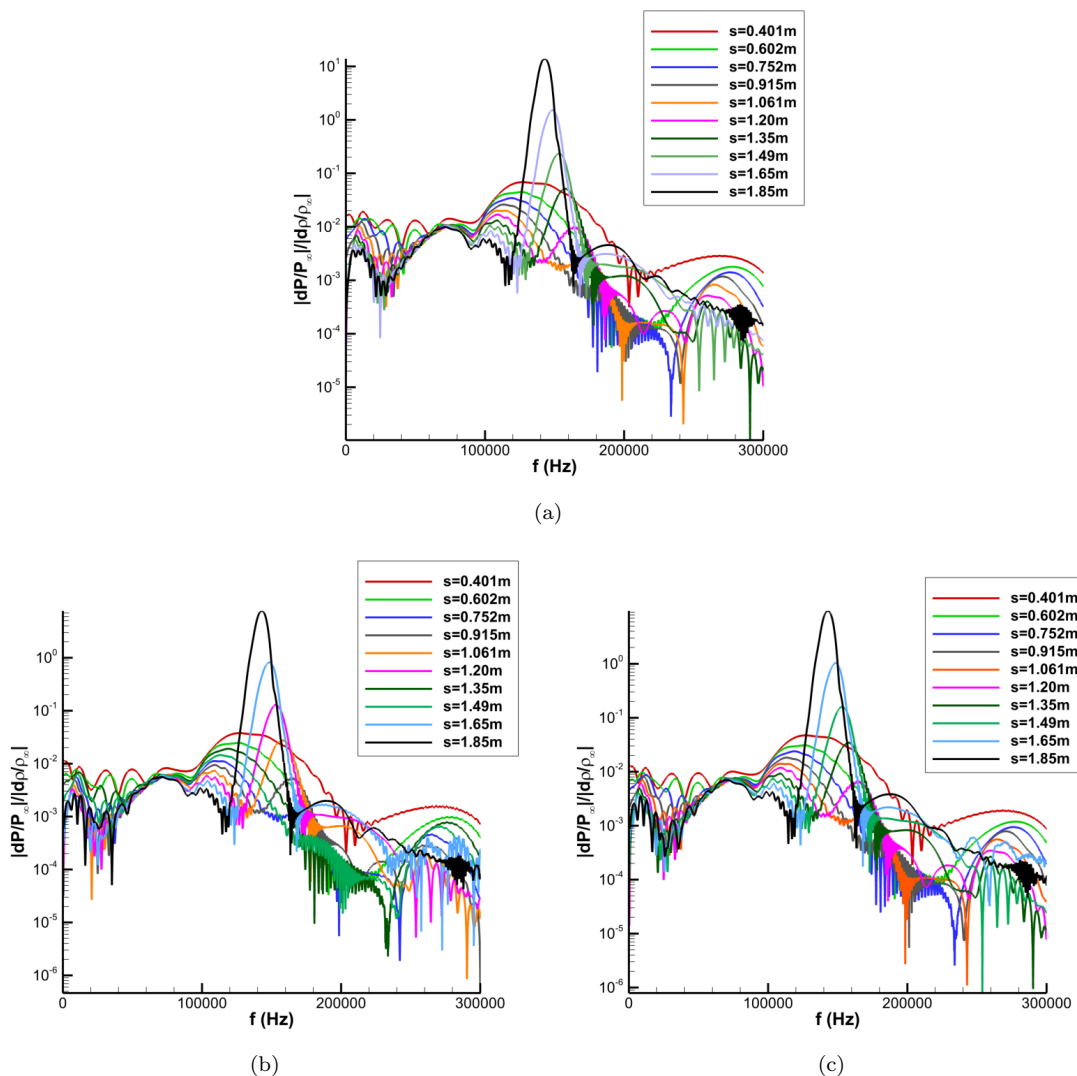

(a)

(b)

(c)

Figure 21. FFT decomposed surface pressure spectra at various streamwise locations for (a) Case B1, (b) Case B2, and (c) Case B3.

The results for Cases B4 and B5 in Figure 22 follow a similar trend. Case B5 shown in Figure 22b follows closely with the behavior observed in the axisymmetric cases, though the low frequency results throughout the sampling locations show significantly more oscillations. These can again be attributed to the additional forcing waves that result from the planar disturbance cases. Furthermore, the disturbance spectrum at the end of the domain shows a stronger secondary peak near 300 kHz that may be attributed to a more strongly excited 3rd mode instability. Case B4 also clearly demonstrates the appearance of strong second mode amplification. However, significant disturbance amplitudes are also observed throughout the high and low frequency spectra. At the $s = 1.061m$ sampling location near the experimental transition location, it is again observed that the 2nd mode disturbance is noticably weaker than disturbances found at 76 kHz and 250 kHz.
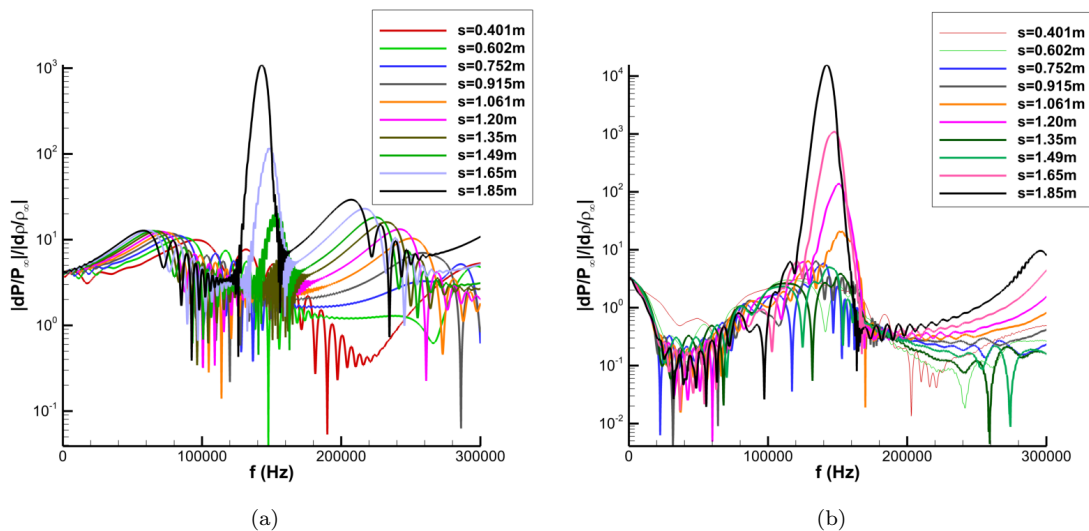
Figure 22. FFT decomposed surface pressure spectra at various streamwise locations for (a) Case B4 and (b) Case B5.

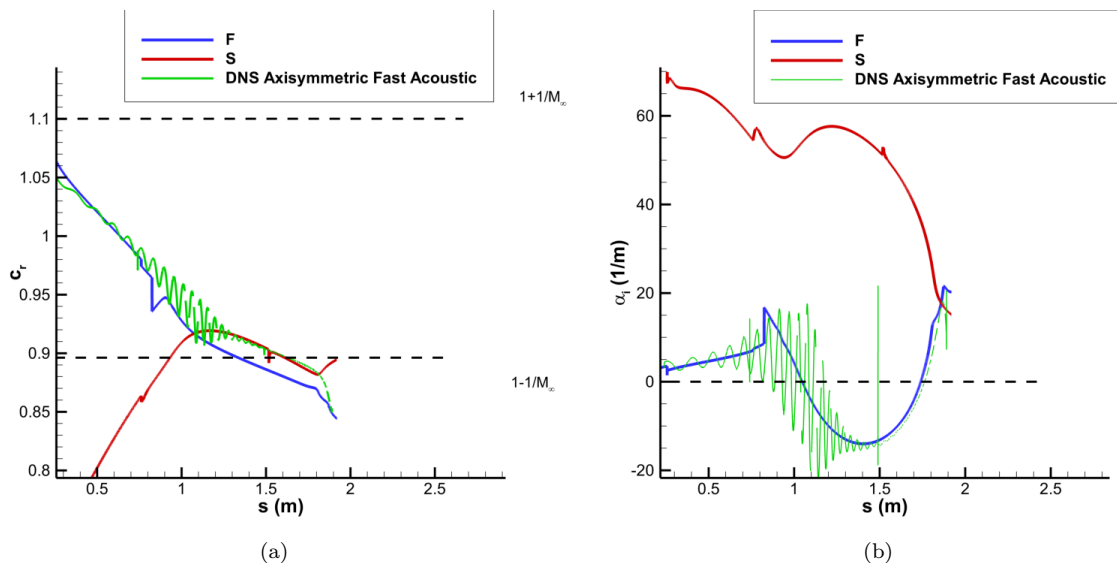## B. Comparison of LST Results with Unsteady DNS

Figure 23. Case B1 unsteady DNS vs. LST predicted results for 150 kHz disturbances (a) Phase Speed (b) Growth Rate.

Through Equations 26, 27, and 28 the Fourier decomposed unsteady DNS can be used to calculate the growth rates and phase speeds of different throughout surface perturbations the disturbance spectrum. These were directly compared to the instability modes predicted by LST. The results for the 150 kHz frequency disturbance for the axisymmetric, fast acoustic (Case B1), slow acoustic (Case B2), and hotspot (Case B3) pulses are presented in Figures 23, 24, and 25 respectively.
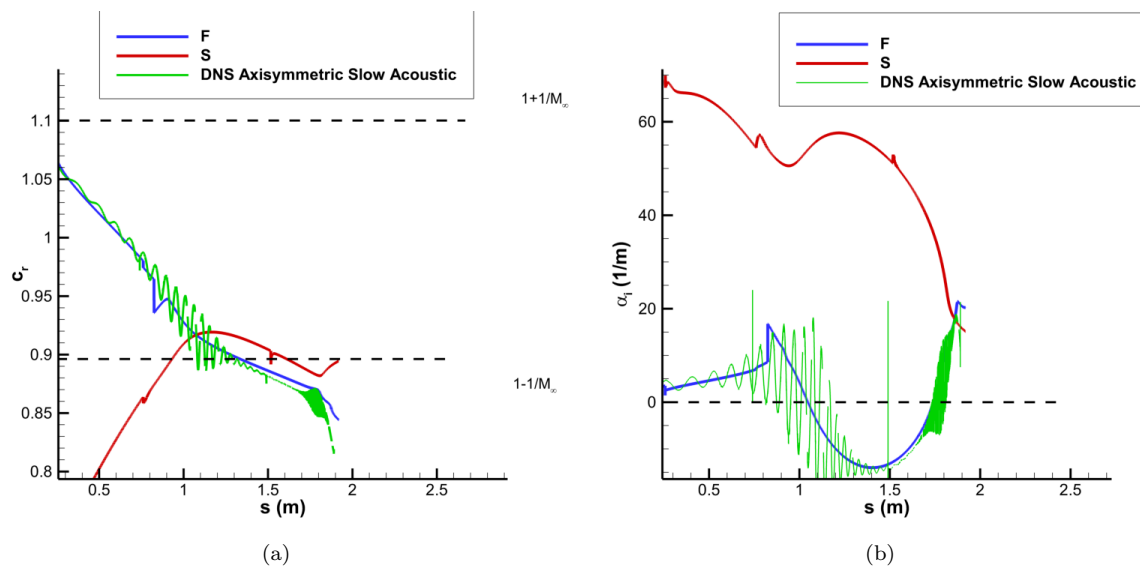
American Institute of Aeronautics and Astronautics

Figure 24. Case B2 unsteady DNS vs. LST predicted results for 150 kHz disturbances (a) Phase Speed (b) Growth Rate.

The unsteady DNS results for case B1 show good agreement with LST, demonstrating that the discrete mode F is unstable for this case. The LST predicts an extensive synchronization range for this frequency between streamwise locations of 1.1 m and 1.8 m. Prior to this synchronization region, significant oscillations in both the phase speed and growth rate plots can be observed in the DNS results. This oscillation is indicative of modal interactions, though it is still apparent that the unstable mode F dominates the flow. These oscillations dampen out significantly as the disturbance propagates through the end of the domain for Case B1 in Figure 23. However, the DNS also shows a rapid destabilization of the 150 kHz disturbance at the end of the domain that the LST seems to under-predict.
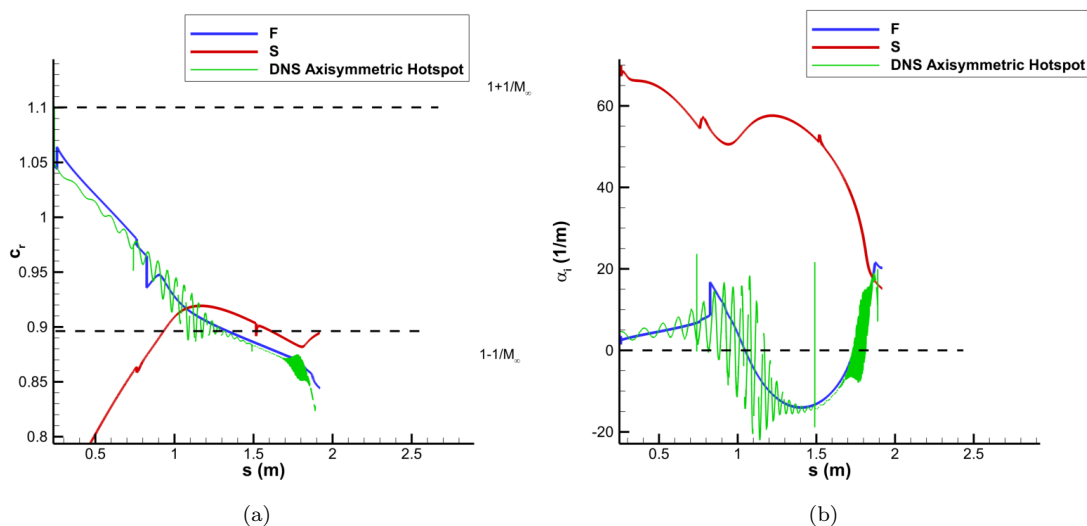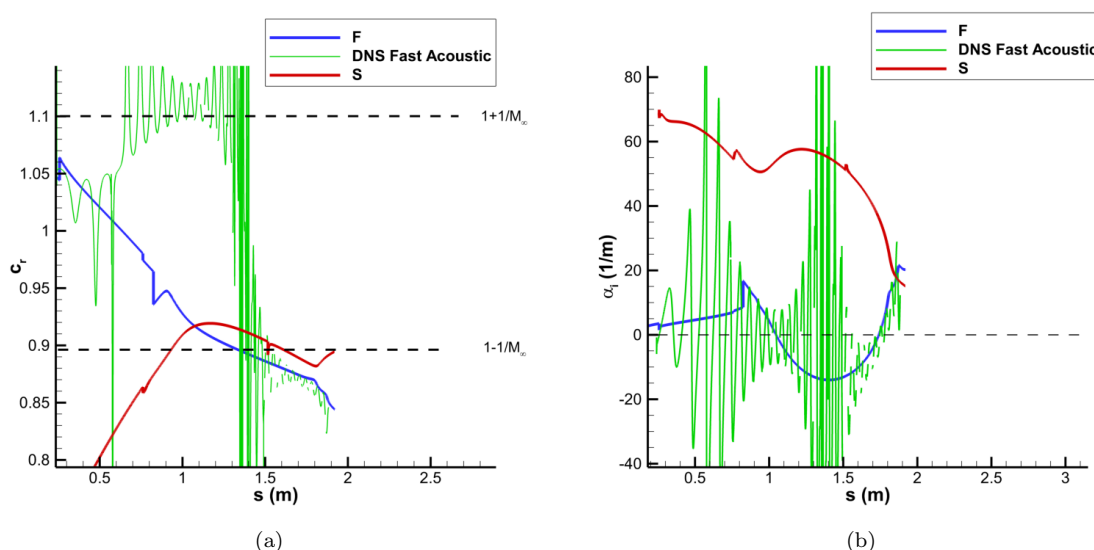

Figure 25. Case B3 DNS vs. LST predicted results for 150 kHz disturbances (a) Phase Speed (b) Growth Rate.

The results for Case B2 in Figure 24 and Case B3 in Figure 25 similarly follow the unstable mode F disturbance, though strong confined oscillations in the unsteady DNS results are also observed at the end of the synchronization between the discrete mode F and mode S at this frequency. The DNS results here also show a rapid destabilization following the end of synchronization at this frequency, contrary to the strong

American Institute of Aeronautics and Astronautics

stable growth rate predicted by the LST. This may be indicative of an additional instability mode that the LST has difficulty capturing. One potential source of downstream instability is the supersonic mode, which is characterized by an an disturbance wave propagating with a phase speed that is supersonic relative to the local mean velocity. This supersonic mode can be observed through acoustic radiation from the boundary layer into the shock layer in the form of decaying mach wave.[38] Figure 12 and Figure 13 show the emergence of some of these radiating mach waves starting near $s = 1.4m$ for the Case B3 and Case B5 respectively. It remains to be seen whether this abrupt change in the DNS growth rates and phase speeds is due to an additional instability mechanism, or simply a numerical oscillation occurring at the branch point of the discrete boundary layer disturbances.

Similarly, the DNS and LST comparisons for the 150 kHz disturbance are given in Figure 26 for Case B4 and Figure 27 for Case B5. The boundary layer disturbances resulting from Case B4 do not seem to become dominated by 2nd mode instabilities until the far downstream regions of the cone. The growth rate shown in Figure 26b is highly oscillatory and centered around a neutrally stable disturbance until approximately $s = 1.6m$. Furthermore, the phase speed plot in Figure 26a shows similar oscillations while a significant section of the unsteady DNS disturbance is centered around the freestream fast acoustic spectrum. The oscillatory nature of these disturbances are again indicative of the influence of multiple coupled modes at these relatively upstream locations. This is likely the influence of the freestream forcing dominating the disturbance field before resonant interactions sufficiently amplify the 2nd mode.

Figure 26. Case B4 unsteady DNS results vs. LST predicted results for 150 kHz disturbances (a) Phase Speed (b) Growth Rate.

The planar slow acoustic case (Case B5) correlates much better with the LST results. Figure 27a shows that the phase speed of the 150 kHz disturbance in the unsteady DNS matches very well with the LST predicted phase speed for the fast acoustic instability at this frequency. The growth rate shown in 27b further corroborates this, though the results prior to 1.4 m still show signifcant oscillations in the DNS results. From this it can be seen that the planar slow acoustic disturbance behaves similarly to the axisymmetric hotspot and acoustic disturbances, and primarily excites the 2nd mode instability at this frequency. The rapid destabilization effect observed in the axisymmetric disturbance cases, however, was not seen at the end of the domain here in for the planar slow acoustic case.
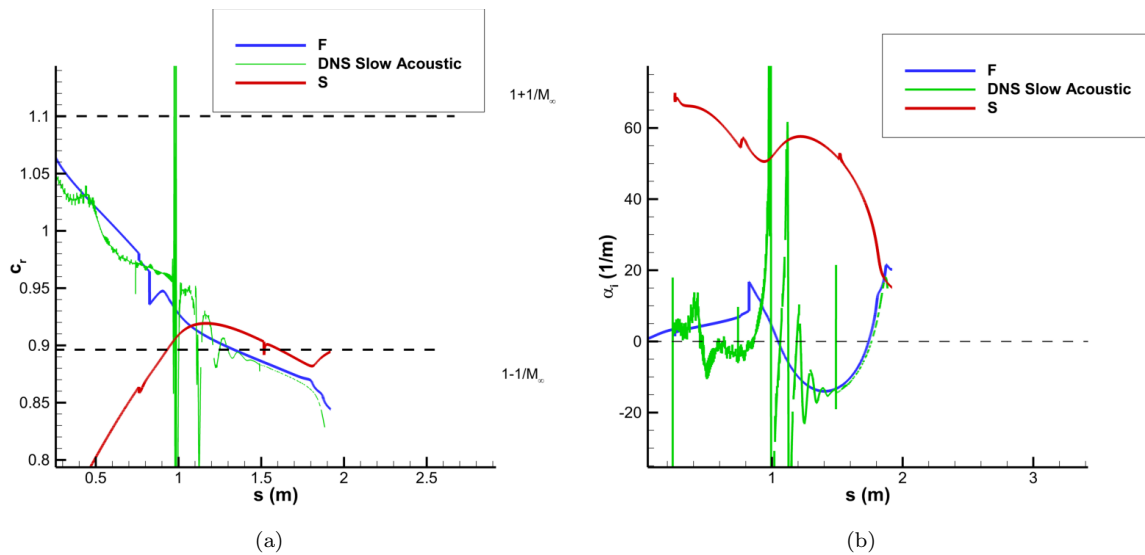
(a)　　　　　　　　　　　　　　　　　　　　　　(b)

Figure 27.　Case B5 unsteady DNS results vs. LST predicted results for 150 kHz disturbances: (a) Phase Speed (b) Growth Rate.

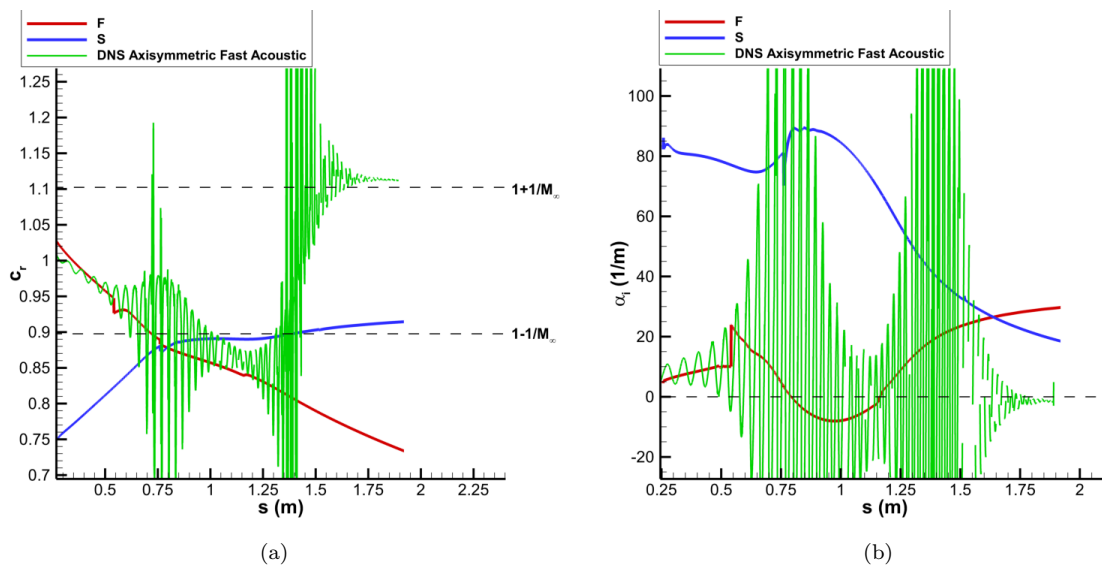

(a)　　　　　　　　　　　　　　　　　　　　　　(b)

Figure 28.　Case B1 unsteady DNS results vs. LST predicted results for 176 kHz disturbances: (a) Phase Speed (b) Growth Rate.

Similar results are presented for the 176 kHz disturbance for Case B1 in Figure 28, for Case B4 in Figure 29, and for Case B5 in Figure 30. This frequency was determined through LST to correspond to the most amplified 2nd mode instability at the experimental transition location. The other axisymmetric disturbance cases at this frequency have been omitted as they share very similar characteristics to Figure 28.

Figure 28a shows that Case B1 generates significant fast acoustic disturbances in the boundary layer upstream on the cone. The boundary layer disturbances then experience strong modulations at the synchronization point and another downstream location before the disturbances become dominated by the fast acoustic waves generated from forcing. The growthrate plot in Figure 28b shows that this second modulation occurs near the branch II neutral point, which indicates that the boundary layer disturbances quickly become dominated by the freestream forcing after the 2nd mode stabilizes for this frequency.
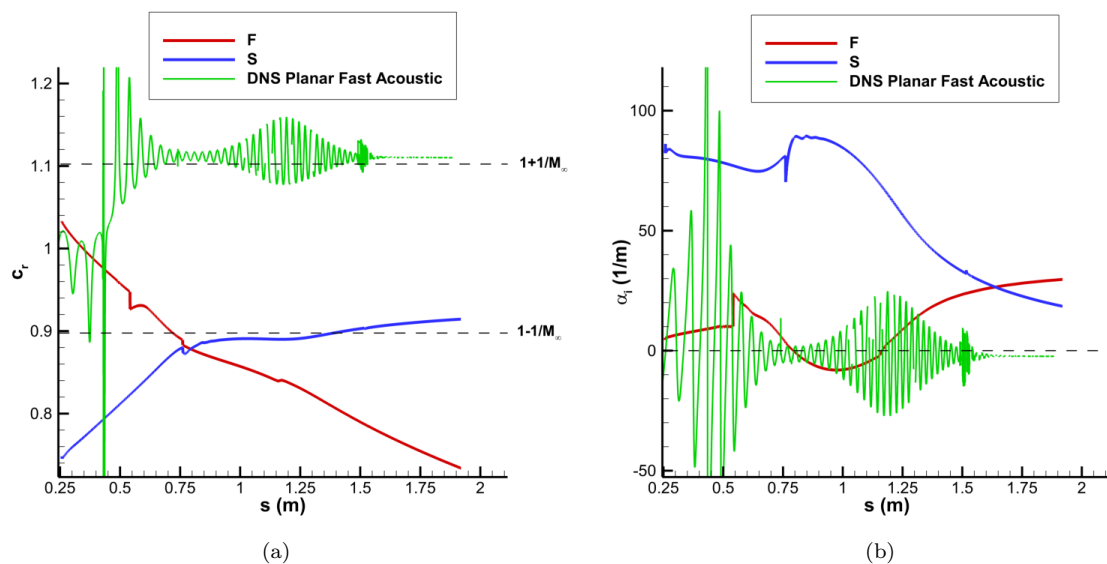
American Institute of Aeronautics and Astronautics

Figure 29. Case B4 unsteady DNS results vs. LST predicted results for 176 kHz disturbances: (a) Phase Speed (b) Growth Rate.
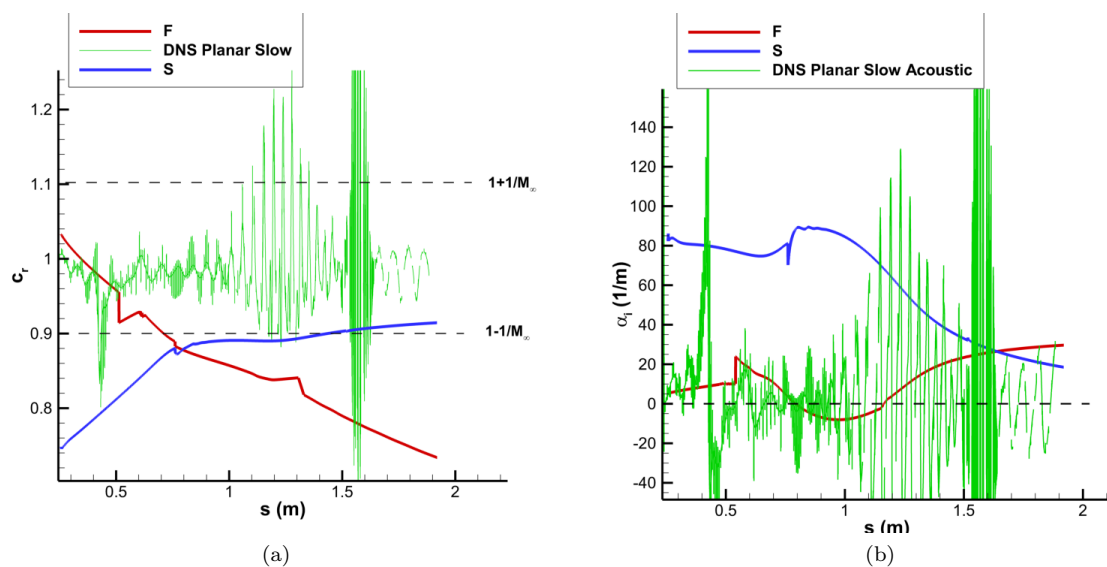

Figure 30. Case B5 unsteady DNS results vs. LST predicted results for 176 kHz disturbances: (a) Phase Speed (b) Growth Rate.

Figure 29a shows a similar behavior for Case B4, though the DNS depicts the boundary layer disturbances tracking the continuous fast acoustic spectrum much further upstream. The growth rate plot in Figure 29b for Case B4 shows the DNS perturbation is largely dominated by a neutrally stable disturbance. Oscillations in this case are centered again around the synchronization point and the branch II neutral point, indicating that while the 2nd mode is not the dominant boundary layer instability at this case, its interactions still affect the instabilities at 176 kHz. This behavior can be attributed to the stronger freestream forcing waves that result from the planar disturbances.

The results in Figure 30 show that Case B5 similarly generates fast acoustic waves upstream on the cone. However, these quickly experience strong modulations and begin tracking the continuous entropy/vorticity spectrum in the phase speed plot in Figure 30a. The growth rate plot in Figure 30b shows strong oscillations near the synchronization and branch II neutral points, similar to Case B4 with what appears to be a

American Institute of Aeronautics and Astronautics

neutrally stable/slightly unstable general boundary layer disturbance. The results indicate that, at least at this frequency of 176 kHz, Case B5 significantly excites entropy disturbances in the boundary layer. This is contrary to the results for Case B5 at 150 kHz and the results for the other cases at both of these frequencies. Thus, the transition in this blunt nose geometry is likely not solely governed by the 2nd mode, and corroborates Marineau's[33] original conclusions regarding this case.

VIII.   Receptivity Results

The primary goal of this study is to calculate and present the receptivity coefficients resulting from a variety of freestream pulse disturbances with broadband, continuous frequency spectra for the current cone geometry. The receptivity coefficient spectra for each of the disturbances was calculated from Equation 29 using surface pressure perturbation data taken from unsteady DNS, as well as N-factor data derived from LST. This method was originally proposed by Huang[20, 21] in order to decompose the perturbation amplitudes and specifically extract the receptivity spectrum of the 2nd mode instability. Furthermore, isolating the contributions of different modal disturbances to the total initial disturbance amplitudes and would allow for greater specificity when tracking the development of instabilities across a flow domain. An example of a more rigorous method for determining the receptivity coefficients for different modal disturbances is the bi-orthogonal decomposition method developed by Tumin[31] and Miselis et al.[32] Miselis et al. showed that this bi-orthogonal decomposition could be used to isolate receptivity coefficients for even more of the different discrete and continuous instability modes in a flow, rather than just the 2nd mode like the method used by Huang and this study. However, this much more rigorous decomposition model requires additional development before it can be applied here.

Using Huang's method, the receptivity coefficients were calculated for each of the disturbance cases. Additionally, we were also able to generate the phase angle spectra for the disturbance cases. With the data from the receptivity coefficient spectra and the phase angle spectra, the total initial receptivity response to a freestream disturbance can be reconstructed. These initial disturbances can then be used as inputs for more advanced transition predicted methods like Mack's amplitude method,[28] Crouch's variable N-factor method,[24] Marineau's iterative method,[29] and Ustinov's implementation of the amplitude methods.[30]

The receptivity coefficient spectra for each of the cases are plotted below in Figures 31 through 33. Additionally, since these receptivity calculations may be sensitive to sampling location,[21] a comparison of the receptivity spectra for different sampling locations was made for each of the axisymmetric and planar disturbances. The receptivity spectra for Case B1 and Case B2 are presented in Figure 31a, while Case 3 is presented in Figure 32.
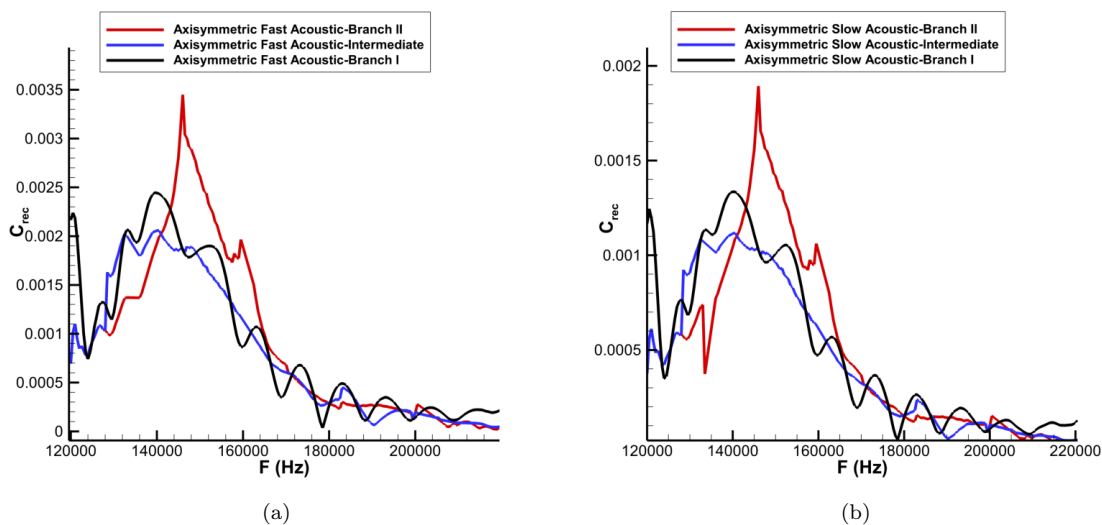

(a)   (b)

Figure 31. Receptivity coefficients at different sampling locations for (a) Case B1 (b) Case B2.

The sampling locations were chosen to be at the branch I neutral stability point x_{brI}, the branch II neutral

American Institute of Aeronautics and Astronautics

stability point x_{brII}, and an intermediate location defined at $x_{sample} = 1.3 * x_{brI}$ for a given frequency. This was chosen to ensure the sampling location remained within the unstable region for the 2nd mode. The branch I point was chosen to compare directly to Balakumar[11] and Huang.[21] Huang stated that simply using the pressure perturbations at the branch I neutral point may cause the signal to be dominated by the multimodal content of the disturbance. This may make it difficult to apply the receptivity results for general transition studies. Figures 31 and 32 however show that 2nd mode disturbances dominate for the freestream axisymmetric pulse cases. While the branch I sampling case does show significantly more oscillations, which are indicative of multimodal disturbances,[21] the general shape and magnitude of the receptivity coefficients is in line with the other sampling locations.

The branch II sampling location spikes near 140 kHz to 150 kHz, which correlates to the most amplified frequencies at the end of the computed domain. This spike may be due to the influence of a potentially unstable supersonic mode in the downstream region of the cone. However, the supersonic mode is only observed far enough downstream that it is unlikely to have an effect on the primary transition observed in the experiment. Additional studies into the impact of the supersonic mode are necessary for this case before its significance can be fully determined. It can be concluded that, for the axisymmetric disturbances studied here so far, sampling location does not have a significant impact on the resulting receptivity coefficients, and the 2nd mode disturbance dominates. This is likely because any extraneous forcing waves are primarily isolated to and damped out in the upstream regions of the cone near the nose. As a result, they do not interfere with the development of 2nd mode disturbances far downstream for these cases.
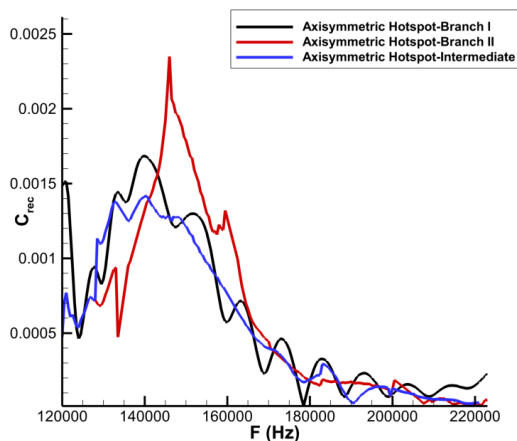

Figure 32.   Case B3 receptivity coefficients for different sampling locations.

The results also show that for axisymmetric pulse disturbances, Case B1 generates the strongest initial disturbance amplitudes followed by Case B3 and then Case B2. This is in line with the LST and unsteady DNS results which show that the unstable 2nd mode corresponds to the discrete mode F originating from the fast acoustic spectrum.

Figure 33 presents the same data for the planar freestream disturbance cases. The receptivity coefficients for the Case B5 show significantly different shapes from the axisymmetric pulse cases. The magnitudes of the receptivity coefficients are also significantly higher. This is because the planar disturbances continually introduce additional perturbations throughout the domain as the shock-disturbance front propagates along with the freestream disturbance. The Fourier decomposition results presented in this study also do not account for the difference in wavenumber distributions between the finite axisymmetric and semi-infinite planar freestream disturbances. Here, Case B5 seemed to again more readily excite the 2nd mode disturbance. Additionally, the Case B5 excited low frequencies much more readily than Cases B1 through B3, likely due to forcing waves again. This can also be seen in the FFT contour shown in Figure 19b. The branch I sampling location shows the influence of this much more significantly, indicating that receptivity results are much more sensitive for planar disturbances to lower frequency forcing waves. On the other hand, the intermediate and branch II sampling locations show very similar results, peaking at frequencies between 125 and 145 kHz, and matches well with the LST prediction.
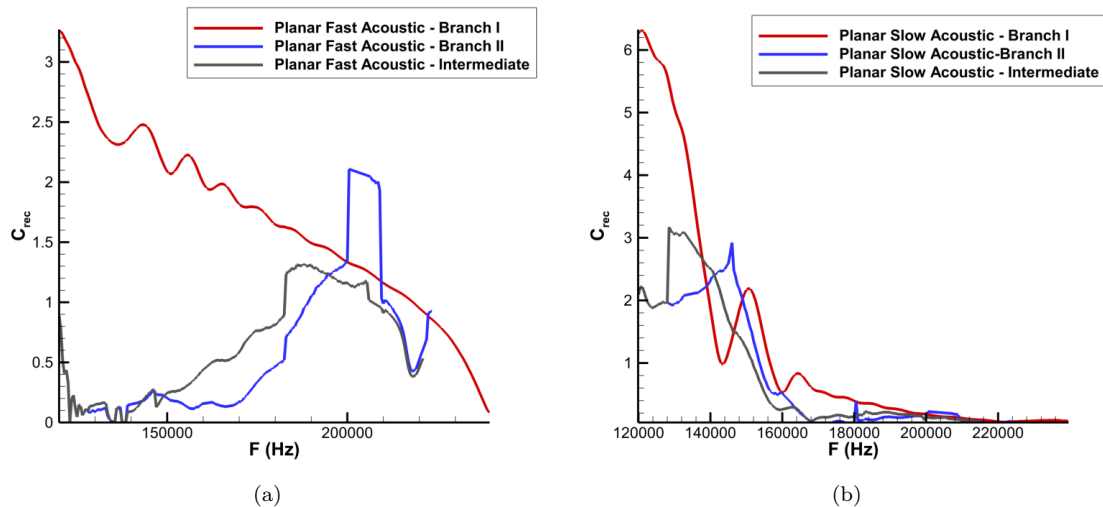
American Institute of Aeronautics and Astronautics

(a)

(b)

Figure 33. Receptivity coefficients at different sampling locations for (a) Case B4 and (b) Case B5.

The results for Case B4 in Figure 33a also differ significantly from the Cases B1 through B3. Here, the branch I sampling location produces a continuous broadband receptivity coefficient distribution, similar in overall shape to our input pulse. This indicates that at this point, the forcing waves excited by the planar fast acoustic pulse are sufficiently strong as to mask the initial 2nd mode instability at the branch I neutral point. The resulting combined disturbances at this location result in disturbance amplitudes far larger than those expected of the pure 2nd mode. The under-prediction of the DNS-derived N-factor in Figure 20b can be attributed to the strong multimodal nature of the DNS disturbance at the branch I neutral point. The other sampling locations also show that the receptivity coefficients are highest near 200 kHz, contrary to the axisymmetric cases. Looking again at Figure 19a it can be seen that an additional band of amplified disturbances can be found at these frequencies. The receptivity results indicate that these disturbance frequencies also are excited very readily in contrast to the LST predicted 2nd mode for this case. The planar results indicate that transition for this intermediate bluntness case is likely not dominated by 2nd mode instabilities for freestream environments with more distributed noise.
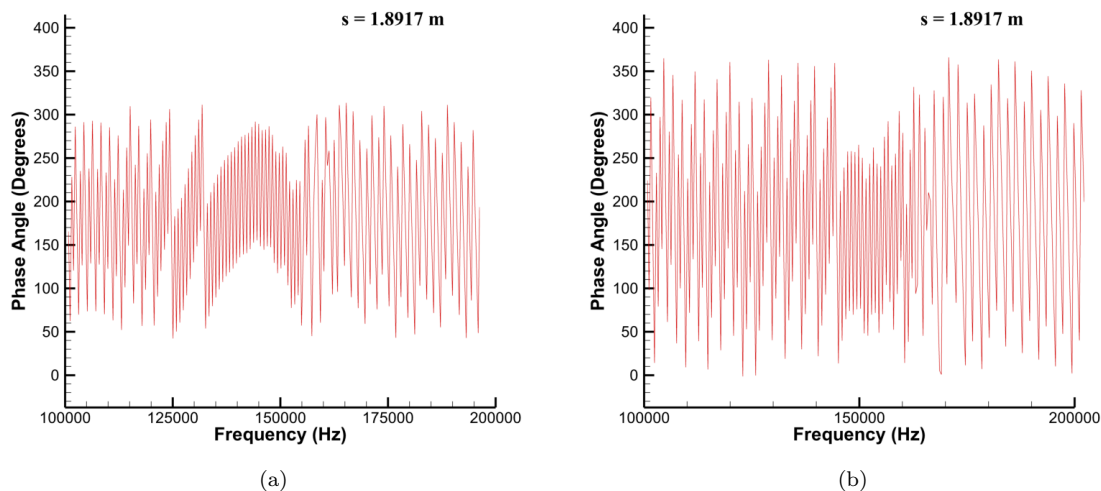

(a)

(b)

Figure 34. Spectral phase angle plots for (a) Case B2 and (b) Case B4.

American Institute of Aeronautics and Astronautics

The phase angle spectra for Case B2 and B4 are also presented in Figure 34. These spectra can also be used to directly identify modes in the flow. A regular pattern occurs in the phase angle distribution until a more coherent structure is formed between frequencies of 135 kHz and 150 kHz in Figure 34a for Case B2, corresponding to the band of the most unstable frequencies at this streamwise location. A similar pattern is seen in Figure 34b between 145 and 155 kHz for Case B4, and throughout the other disturbances as well. Using the receptivity coefficients in Figure 31 through Figure 33 along with phase angle spectra, such as those presented in Figure 34, the initial disturbance response to a freestream perturbation can be reconstructed.[21]

IX. Discussion

The receptivity of a 7-degree half-angle, 9.525 mm nose radius cone at mach 10 to a variety of freestream, continuous broadband frequency disturbances was investigated in this study. The goals of this study were to investigate the receptivity mechanism in this blunt cone flow, and to produce receptivity coefficient spectra for a variety of continuous broadband frequency disturbances. Generating an extensive database of these receptivity coefficients would provide improved freestream noise response data to replace the empirical correlations being used in improved transition prediction methods such as Mack's amplitude method,[28] Crouch's variable N-factor method,[24] and the improved amplitude methods developed by Marineau[29] and Ustinov.[30] Similar to Huang,[20,21] this study focused on obtaining the receptivity coefficients associated with the amplified 2nd mode instability, which in this case corresponded to the discrete mode F disturbance.

This process first involved converging the steady meanflow using a high-order shock-fitting method. This steady solution was then perturbed with freestream axisymmetric fast acoustic (Case B1), slow acoustic (Case B2), and hotspot (Case B3) disturbances. It was also perturbed with freestream planar fast acoustic (Case B4) and slow acoustic (Case B5) disturbances. These freestream disturbances were modelled as Gaussian pulses to approximate the continuous, broadband frequency nature of noise found in experimental as well as flight conditions. LST analysis was also performed on the meanflow and used to derive disturbance amplification rates, or N-factors, for the 2nd mode. Finally, using the LST-derived N-factors and the FFT decomposed unsteady data, the receptivity coefficients for the 2nd mode were extracted from the total disturbance spectra for each of the cases.

The LST analysis showed that boundary layer disturbances in a band of frequencies extending from approximately 118 kHz to 238 kHz experienced 2nd mode growth. Furthermore, the unstable 2nd mode in this case was found to be the discrete mode F, originating from the continuous fast acoustic spectrum. The N-factor curve derived from LST in this study agrees well with the PSE-derived N-factor curve presented by Marineau, and the most unstable frequency at the experimental transition location of $s = 1.037m$ was determined by LST to be 176 kHz. LST analysis predicted an N-factor of 1.7 at this location, compared to Marineau's[33] reported N-factor of 1.6.

Unsteady DNS results showed that all five of the freestream disturbance cases were capable of exciting significant 2nd mode disturbances in the boundary layer. Cases B1, B2, and B3 agreed well with LST for the 150 kHz frequency cases, though significant differences between the DNS and LST were observed for the 176 kHz disturbance. Similarly, Case B5 also agreed well with LST at 150 kHz, though Case B4 showed evidence of significant modal interactions with fast acoustic forcing waves. Case B5 excited significant entropy disturbances in the boundary layer at 176 kHz, but excited fast acoustic 2nd mode disturbances at lower frequencies. The PSD contours for Case B5, and Case B4 in particular, showed significant additional disturbances that can be associated with these additional freestream forcing waves. In particular, the planar fast acoustic pulse in Case B4 resulted in significant disturbance amplitudes at frequencies of 76 kHz and 252 kHz, outside of the standard unstable 2nd mode region predicted by LST at the experimental transition location. This indicates that distributed broadband freestream disturbances, like Cases B4 and B5 here, may excite strong disturbances outside of the 2nd mode which can significantly impact transition. Unsteady DNS also showed the development of mach wave-like acoustic radiation from the boundary layer disturbances downstream on the cone. This phenomenon is characteristic of supersonic mode instabilities. Further study is required to determine the significance of the supersonic mode in this case.

Receptivity coefficients for 2nd mode disturbances were also calculated for all five disturbance cases. It was found that the results were generally independent of sampling location for the axisymmetric disturbances in Cases B1, B2, and B3. Case B1 generated the largest receptivity coefficients, followed by Case B3 and then Case B2. The planar disturbances in Case B4 and Case B5 were found to be much more sensitive

to sampling methodology, as the perturbation at the branch I neutral point is a combination of all of the boundary layer disturbances introduced continuously by the shock-disturbance interaction. Prior to amplification, the 2nd mode may not necessarily dominate at this point. This caused the branch I sampled case to have much higher, and much more oscillatory receptivity coefficient distribution. The N-factor normalization method was shown to more readily extract initial amplitudes for the 2nd mode disturbance for these planar disturbance cases. Though, the results for Case B4 did not follow the expected trend for a 2nd mode instability and indicated that the 2nd mode is not necessarily dominant in determining transition for this blunt nose case. Additionally, it was shown that the disturbance phase angles could also be extracted. Using the receptivity coefficients and phase angle data, the initial amplitude response to freestream noise cases should be able to be constructed.

X.   Conclusion

The receptivity coefficients for a variety of continuous, broadband frequency disturbances has been investigated in a Mach 10 flow over a blunt cone at $0°$ angle of attack. However, in order to fully encompass the large envelope of disturbances found in experimental and real flight conditions, the receptivity response to many more different freestream disturbances must be tested. These include planar hotspot as well as axisymmetric and planar vorticity waves. In future studies, the receptivity response to more complex continuous frequency freestream disturbances will also be modelled using a pulse model. These freestream disturbances include off-axis and oblique pulses and would necessitate the expansion of the current axisymmetric meanflow to fully simulate the development of three-dimensional perturbations. Additional geometries must also be studied in order to complete the receptivity database, with the sharper nose geometries based on Run 3742 and Run 3746 in the experiment by Marineau et al.[33] being of particular interest.

Overall, it was shown that continuous frequency freestream disturbances could be modelled using Gaussian pulses, and that these pulse disturbances could significantly excite modal instabilities. The instabilities introduced through unsteady DNS were shown to match well with LST predicted instability modes far downstream on the cone. The receptivity coefficient spectra for each of the freestream disturbance cases was also successfully found. The receptivity coefficients for the axisymmetric cases showed that the resulting boundary layer instabilities were dominated by the 2nd mode in these cases, while the planar disturbance cases showed that forcing waves generate signfcant multimodal behaviors in the perturbations. These results offer a much more precise measurement of the flow response to freestream noise than empirical correlations, and will be useful when developing improved transition prediction methods.

Acknowledgments

References

[1]Fedorov, A., "Transition and Stability of High-Speed Boundary Layers," *Annual Review of Fluid Mechanics*, Vol. 43, 2011, pp. 79–95.

[2]Reshotko, E., "Hypersonic Stability and Transition," *Hypersonic flows for reentry problems*, Vol. 1, No. A93-42576 17-02, 1991, pp. 18–34.

[3]Zhong, X. and Wang, X., "Direct Numerical Simulation on the Receptivity, Instability, and Transition of Hypersonic Boundary Layers," *Annual Review of Fluid Mechanics*, Vol. 44, 2012, pp. 527–561.

[4]Ma, Y. and Zhong, X., "Receptivity of a Supersonic Boundary Layer over a Flat Plate. Part 3. Effects of Different Types

of Free-stream Disturbances," *Journal of Fluid Mechanics*, Vol. 532, 2005, pp. 63–109.

[5]Mack, L. M., "Boundary layer stability theory," Tech. Rep. 900-277, JPL Report, 1969.

[6]Ma, Y. and Zhong, X., "Receptivity of a supersonic boundary layer over a flat plate. Part 1. Wave structures and interactions," *Journal of Fluid Mechanics*, Vol. 488, 2003, pp. 31–78.

[7]Ma, Y. and Zhong, X., "Receptivity of a supersonic boundary layer over a flat plate. Part 2. Receptivity to freestream sound," *Journal of Fluid Mechanics*, Vol. 488, 2003, pp. 79–121.

[8]Fedorov, V., "Receptivity of a High-Speed Boundary Layer to Acoustic Disturbances," *Journal of Fluid Mechanics*, Vol. 491, 2003, pp. 101–129.

[9]Fedorov, A. V., Ryzhov, A. A., Soudakov, V. G., and Utyuzhnikov, S. V., "Receptivity of a high-speed boundary layer to temperature spottiness," *Journal of Fluid Mechanics*, Vol. 722, 2013, pp. 533–553.

[10]Balakumar, P. and Kegerise, M., "Receptivity of Hypersonic Boundary Layers to Acoustic and Vortical Disturbances," *AIAA-2011-371*, 2011.

[11]Balakumar, P. and Chou, A., "Transition Prediction in Hypersonic Boundary Layers Using Receptivity and Freestream Spectra," *AIAA Journal*, Vol. 56, No. 1, 2018, pp. 2593–2606.

[12]Kara, K., Balakumar, P., and Kandil, O., "Effects of Nose Bluntness on Hypersonic Boundary-Layer Receptivity and Stability over Cones," *AIAA Journal*, Vol. 55, No. 12, 2011, pp. 2593–2606.

[13]Lei, J. and Zhong, X., "Numerical Simulation of Freestream Waves Receptivity and Breakdown in Mach 6 Flow over Cone," *AIAA-2013-2741*, 2013.

[14]Fedorov, A. and Tumin, A., "High-Speed Boundary-Layer Instability: Old Terminology and a New Framework," *AIAA Journal*, Vol. 49, No. 8, 2011, pp. 1647–1657.

[15]Mack, L. M., "Boundary Layer Linear Stability Theory," Tech. rep., AGARD report No. 709, 1984.

[16]Zhong, X. and Ma, Y., "Boundary-Layer Receptivity of Mach 7.99 Flow over a Blunt Cone to Free-Stream Acoustic Waves," *Journal of Fluid Mechanics*, Vol. 556, 2006, pp. 55–103.

[17]Lei, J. and Zhong, X., "Linear Stability Analysis of Nose Bluntness Effects on Hypersonic Boundary Layer Transition," *Journal of Spacecraft and Rockets*, Vol. 49, No. 1, 2012, pp. 24–37.

[18]Reshotko, E. and Tumin, A., "Role of Transient Growth in Roughness-Induced Transition," *AIAA Journal*, Vol. 42, No. 4, 2004, pp. 766–774.

[19]Schneider, S., "Effects of High-Speed Tunnel Noise on Laminar-Turbulent Transition," *Journal of Spacecraft and Rockets*, Vol. 38, 2001, pp. 323–333.

[20]Huang, Y. and Zhong, X., "Effects of Nose Bluntness on Hypersonic Boundary-Layer Receptivity and Stability over Cones," *AIAA Journal*, Vol. 52, No. 12, 2014, pp. 2652–2672.

[21]Huang, Y., *Numerical Study of Hypersonic Boundary-Layer Receptivity and Stability with Freestream Hotspot Perturbations*, Ph.D. thesis, 2016.

[22]Schneider, S., "Developing Mechanism-Based Methods for Estimating Hypersonic Boundary-Layer Transition in Flight: The Role of Quiet Tunnels," *Progress in Aerospace Sciences*, Vol. 72, 2015, pp. 17–29.

[23]Chang, C., Malik, M., Erlebacher, G., and Hussaini, M., "Compressible stability of growing boundary layers using parabolized stability equations," *22nd Fluid Dynamics, Plasma Dynamics and Lasers Conference*, 1991.

[24]Crouch, J. and Ng, L., "Variable N-Factor Method for Transition Prediction in Three-Dimensional Boundary Layers," *AIAA Journal*, Vol. 38, No. 2, 2000.

[25]Reed, H. L., Saric, W. S., and Arnal, D., "Linear Stability Theory Applied to Boundary Layers," *Annual Review of Fluid Mechanics*, Vol. 28, No. 1, 1996, pp. 389–428.

[26]Duan, L., Choudhari, M. M., and Zhang, C., "Pressure fluctuations induced by a hypersonic turbulent boundary layer," *Journal of Fluid Mechanics*, Vol. 804, 2016, pp. 578–607.

[27]Sivasubramanian, J. and Fasel, H. F., "Direct numerical simulation of transition in a sharp cone boundary layer at Mach 6: fundamental breakdown," *Journal of Fluid Mechanics*, Vol. 768, 2015, pp. 175–218.

[28]Mack, L. M., "Transition Prediction and Linear Stability Theory," Tech. rep., AGARD CP-224, 1977.

[29]Marineau, E., "Prediction Methodology for Second-Mode dominated Boundary-Layer Transition in Wind Tunnels," *AIAA Journal*, Vol. 55, No. 2, 2017.

[30]Ustinov, M. V., "Amplitude method of prediction of laminar-turbulent transition on a swept-wing," *Fluid Dynamics*, Vol. 52, No. 1, Jan 2017, pp. 71–87.

[31]Tumin, A., "Three-Dimensional Spatial Normal Modes in Compressible Boundary Layers," *Journal of Fluid Mechanics*, Vol. 586, 2007, pp. 295–322.

[32]Miselis, M., Huang, Y., and Zhong, X., "Modal Analysis of Receptivity Mechanisms for a Freestream Hot-Spot Perturbation on a Blunt Compression-Cone Boundary Layer," *AIAA-2016-3345*, 2016.

[33]Marineau, E., Moraru, C., Lewis, D., Norris, J., and Lafferty, J., "Mach 10 Boundary-Layer Transition Experiments on Sharp and Blunted Cones," *AIAA-2014-3108*, 2014.

[34]Zhong, X., "High-Order Finite-Difference Schemes for Numerical Simulation of Hypersonic Boundary-Layer Transition," *Journal of Computational Physics*, Vol. 144, No. 2, 1998, pp. 662–709.

[35]Malik, M. R., "Numerical Methods for Hypersonic Boundary Layer Stability," *Journal of Computational Physics*, Vol. 86, 1990, pp. 376–413.

[36]Aleksandrova, E., Novikov, A., Utyuzhnikov, S., and Fedorov, A., "Experimental Study of the Laminar-Turbulent Transition on a Blunt Cone," *Journal of Applied Mechanics and Technical Physics*, Vol. 55, No. 3, 2014, pp. 375–385.

[37]Lei, J. and Zhong, X., "Linear Stability Analysis of Nose Bluntness Effects on Hypersonic Boundary Layer Transition," *AIAA-2010-898*, 2010.

[38]Knisely, C. P. and Zhong, X., "Significant Supersonic Modes and the Wall Temperature Effect in Hypersonic Boundary Layers," *AIAA Journal*, 2019.

American Institute of Aeronautics and Astronautics

³⁹Knisely, C. P. and Zhong, X., "Sound radiation by supersonic unstable modes in hypersonic blunt cone boundary layers. I. Linear stability theory," *Physics of Fluids*, Vol. 31, No. 2, 2019, pp. 024103.

⁴⁰Knisely, C. P. and X., Z., "Sound radiation by supersonic unstable modes in hypersonic blunt cone boundary layers. II. Direct numerical simulation," *Physics of Fluids*, Vol. 31, No. 2, 2019, pp. 024104.

⁴¹Mortensen, C. H., "Toward an understanding of supersonic modes in boundary-layer transition for hypersonic flow over blunt cones," *Journal of Fluid Mechanics*, Vol. 846, 2018, pp. 789–814.